

Nanoscale Advances

Accepted Manuscript

This article can be cited before page numbers have been issued, to do this please use: P. C. Kumar, S. Mohanty, S. Supriya, R. Swain, J. Kumar and R. Naik, *Nanoscale Adv.*, 2026, DOI: 10.1039/D5NA01136A.



This is an Accepted Manuscript, which has been through the Royal Society of Chemistry peer review process and has been accepted for publication.

Accepted Manuscripts are published online shortly after acceptance, before technical editing, formatting and proof reading. Using this free service, authors can make their results available to the community, in citable form, before we publish the edited article. We will replace this Accepted Manuscript with the edited and formatted Advance Article as soon as it is available.

You can find more information about Accepted Manuscripts in the [Information for Authors](#).

Please note that technical editing may introduce minor changes to the text and/or graphics, which may alter content. The journal's standard [Terms & Conditions](#) and the [Ethical guidelines](#) still apply. In no event shall the Royal Society of Chemistry be held responsible for any errors or omissions in this Accepted Manuscript or any consequences arising from the use of any information it contains.

Diffusion-Induced Enhanced Photoresponsivity, Detectivity in Ag_2S and In_2Se_3 Heterostructure for UV-Visible Photodetector: An Experimental and Computational Analysis

Prabhukrupa Chinmay Kumar¹, Subhashree Mohanty², Swikruti Supriya¹, Rojalin Swain³, Jagdish Kumar^{3,4}, Ramakanta Naik^{1*}

¹Department of Engineering and Materials Physics, Institute of Chemical Technology-Indian Oil Odisha Campus, Bhubaneswar, 751013, India

²Faculty of Science, Sri Sri University, Cuttack, 754006, India

³Department of Physics, Center of Excellence in High Energy and Condensed Matter Physics, Utkal University, Bhubaneswar 751004, India

⁴Department of Physics and Astrophysics, University of Delhi, Delhi-110007, India

*Corresponding author: ramakanta.naik@gmail.com

Abstract:

For recent optical communication and imaging systems, photodetectors are playing a pivotal role. Metal chalcogenide-based photodetectors are widely used for visible light photodetection. In this regard, the In_2Se_3 and Ag_2S combined heterostructure is a promising candidate for Visible light photodetection. The annealing-induced Ag_2S diffusion into the In_2Se_3 layer resulted in a high-performance photo detectivity of 7.32×10^9 Jones. It shows the highest photocurrent during both the rise (62.35 nA) and decay (67.74 nA) phases, coupled with a strong $I_{\text{on}}/I_{\text{off}}$ ratio of 3.96 (rise) and 3.18 (decay). Its rise and fall times ($\tau_r = 7.15$ s, $\tau_d = 6.35$ s) are moderate and well-balanced, suggesting efficient charge separation and recombination kinetics. The bandgap of the annealed film increased with the reduction of structural disorder as probed from the UV-Visible spectroscopy and well supported by the DFT result. The amorphous to polycrystalline phase transformation induced surface morphology change, reduced the contact angle, thus decreasing the hydrophobicity. The refractive index decreased with an increase in optical transmission and skin depth, while optical density reduced upon annealing. The X-ray photoelectron spectroscopy revealed the oxidation states of the elements, while energy dispersive X-ray analysis presented the elemental composition in the films. The heterostructure formation and its mixing upon annealing are viewed from the cross-sectional FESEM images, and the presence of the planes was noticed through HRTEM images. The observed optical properties, along with the enhanced photodetection, pave the way toward the construction of novel III-VI metal chalcogenide-based heterojunctions for high-performance and broadband photodetectors.

Keywords: $\text{Ag}_2\text{S}/\text{In}_2\text{Se}_3$ heterostructure; Photodetector; Optoelectronics; Bandgap; Surface wettability.

1. Introduction

View Article Online
DOI: 10.1039/D5NA01136A

The recent requirement demands cost-effective and less toxic material-based high-speed, highly sensitive photodetectors, based on thin films [1]. Thin films are very useful for visible light photo detection. The semiconducting thin films have a wide range of photodetection applications based on their exceptional optoelectronic properties [2-4]. The factors that influence the photodetector performance are response time, detectivity, responsivity, and wavelength range of detection [5,6]. For various applications in instrumentation and industrial purposes, the photo response in the visible and ultraviolet (UV) regimes has gained attention in recent times. It is basically used for image sensing, chemical analysis, radiation detection, environmental monitoring, optical communications, medical diagnostics, astronomical studies, etc. [7]. Photodetectors (PDs), are the most valuable optoelectronic components in recent days. Its principle is based on the transformation of optical energy into electrical one by photoelectric effect [8]. The ultimate aim of recent methods is to have highly efficient, larger spectral range, high-speed photodetectors from less expensive materials, as well as a low-cost fabrication method. For this purpose, the present study relies on the metal-based chalcogen materials.

The binary combinations from the IIIA-VIA group elements formed compounds basically In-based alloys such as In_2S_3 , InSe , and In_2Se_3 have great importance and are widely used for photodetection applications [9-11]. The important aspects of these combinations include controlled morphology, tunable bandgap, flexibility, good stability, 2D structure, carrier mobility, and remarkable fundamental properties. The 2D materials also have very good light-matter interaction with excellent optoelectronic properties. However, in recent times, the heterostructure films have been widely used for photodetector applications in a broad wavelength scale. For a wider spectral range, the stacking of $\alpha\text{-In}_2\text{Se}_3$ with any 2D semiconducting alloy is a good choice for achieving speedy photo response. The $\alpha\text{-In}_2\text{Se}_3/\text{Si}$ heterojunction acts as a highly efficient heterojunction-based photodetector used for photoelectric imaging and object recognition [12]. The $\alpha\text{-In}_2\text{Se}_3/\text{Ta}_2\text{NiSe}_5$ heterojunction-based photodetector works both under bias voltage state and self-driven state. The detection waveband covers between 405-1550 nm with a response time of only 25 μs [13]. The $\alpha\text{-In}_2\text{Se}_3/\text{WSe}_2$ heterostructure-based photodetector has detectivity and photoresponsivity of 4.34×10^{14} Jones and $4.61 \times 10^5 \text{ A W}^{-1}$ [14]. The self-powered $\gamma\text{-In}_2\text{Se}_3/\text{p-Si}$ heterojunction-based photodetector has enhanced photoresponsivity of 47.9 mA/W, photosensitivity of 282, and photo detectivity of 8.45×10^{10} Jones. The heterostructure explores humidity and light-intensity-dependent photo response [15]. The partially gated $\text{MoS}_2/\alpha\text{-In}_2\text{Se}_3$ heterojunction photodetector shows excellent photo response performance and a non-volatile photo memory

effect. This is suitable for applications like non-volatile memory and other optoelectronic applications involving designing 2D ferroelectric devices[16]. The photo response in the 650-900 nm range is shown by a $\text{WSe}_2/\text{In}_2\text{Se}_3$ heterojunction-based photodetector with good optoelectronic performance at room temperature. The direct band gap multilayer material-based 2D vdW heterojunctions are suitable for future optoelectronic devices [17]. The photo response of $\text{In}_2\text{Se}_3/\text{MoS}_2$ heterojunction photodetector is up to 1310 nm. Here, the photocurrent generation mechanism shifts from photogating to photoconductive effect [18]. The observation of no persistent photoconductivity with fast transient response is observed from p-GaN/ α - In_2Se_3 heterojunction-based UV/Near-IR dual-band photodetector. The formation of α - In_2Se_3 along with a wide bandgap semiconductor-based heterostructure is used for a special type of optoelectronic device [19].

The different energy treatments on such a heterostructure bring modifications for better performances that include ion irradiation, laser irradiation, annealing, etc [20-22]. $\text{In}_2\text{Se}_3/p$ -Si heterojunction photodetectors show enhanced performance at increased argon ion fluence. It brings out higher photosensitivity, photoresponsivity, and photo detectivity with faster rise and decay time. It shows good response to radiation hardening and is used for developing space-based photodetectors [20]. The excitation wavelength of 638 nm at 10 nW laser power and 1500s by $\text{In}_2\text{Se}_3/\text{PtSe}_2$ photodetector resulted in a fast response broadband photodetector. Such a photodetector is suitable for low-energy consumption and high-capacity optoelectronic devices [21]. The thermal annealing on SnS-based thin film resulted in the specific detectivity of 6.8×10^{10} Jones, which is nearly two orders of magnitude greater than that of the unannealed film [22]. In our earlier work, the annealing effect on the Ag_2S -based In_2Se_3 heterostructure film of 800 nm resulted in remarkable photodetection ability with 2.01×10^{-1} A/W responsivity and detectivity of 7.32×10^9 Jones. The nA to mA current increase with 250 °C annealing dramatically enhanced the photo response [23]. The current study relies on the low-thickness-based $\text{Ag}_2\text{S}/\text{In}_2\text{Se}_3$ heterojunction thin film annealed at various temperatures to probe the optimized performance. The annealed heterostructure was subjected to various experimental tools like X-ray diffraction (XRD), X-ray photoelectron spectroscopy (XPS), cross-sectional field emission scanning electron microscopy (FESEM), and photo response study. The experimental results is supported by the density functional theory (DFT) based calculation.

2. Experimental details

2.1. Thin film deposition and thermal annealing

The formation of a bilayer structure of Ag_2S and In_2Se_3 was carried out by the thermal evaporation technique. The HHV Smart coat 3.0 unit was employed for coating of the two

View Article Online
DOI: 10.1039/DNNA01136A

layers from high-purity (99.999% Sigma Aldrich) Ag_2S and In_2Se_3 on a cleaned glass substrate. The rate of deposition was slow (5\AA/sec) for uniformity and homogeneity. The attached thickness controller determines the thickness deposited, and the substrate holder was rotated slowly inside the chamber. The ~ 150 nm of Ag_2S layer was deposited onto ~ 450 nm of In_2Se_3 layer under high vacuum state (10^{-5} Torr). The preparation was done under normal conditions only. The coated films were then cut into pieces for annealing at different temperatures. The diffusion of Ag_2S inside the In_2Se_3 layer was carried out by heat treatment. The hot air oven was used for thermal annealing at $100\text{ }^\circ\text{C}$, $150\text{ }^\circ\text{C}$, $200\text{ }^\circ\text{C}$ and $250\text{ }^\circ\text{C}$ temperatures. The time duration of annealing was 2 hrs inside the oven.



Scheme 1: Annealing of the films at different temperatures

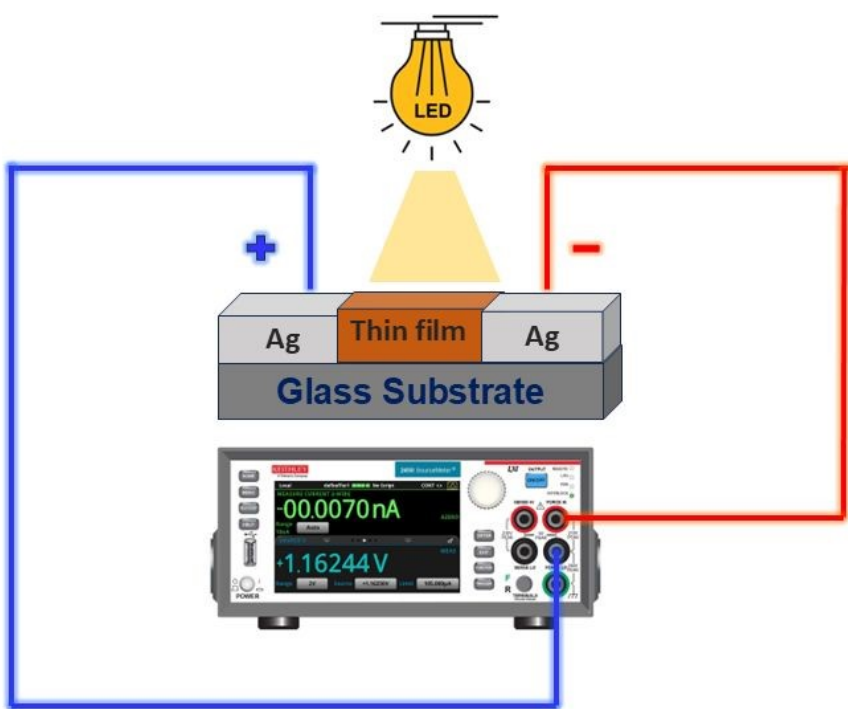
2.2. Experimental characterizations

The thermally annealed films were subjected to different types of experiments, like XRD, FESEM, XPS, Energy dispersive X-ray analysis (EDS), Contact angle, UV-Visible spectroscopy, and IV measurement. The formation of the heterostructure was first checked through cross-sectional FESEM by a JEOL-JSM-7610F unit. The structure of the as-deposited and annealed bilayer was determined through a Bruker D8 Advance XRD unit. The scanning was from $10\text{--}80\text{ }^\circ$ with a $0.03\text{ }^\circ/\text{sec}$ scan rate. Further structural data were collected from HRTEM. The TEM and SAED images were taken by the JEOL HRTEM unit at different scales. The film composition after preparation and annealing was tested by the EDS unit at a high vacuum state (9×10^{-5} Torr vacuum) at 16 kV voltage. The surface morphology pictures were recorded from a JEOL FESEM unit at different scale bars with high magnifications. The optical data were recorded by a JASCO-770 spectrometer with 1 nm resolution from 500 to

2500 nm wavelength range. The surface wettability test was done by the contact angle meter (DME 211 Plus make). The chemical state of the elements was probed through XPS by Axis Ultra, Kratos Analytical instrument. It has Al K_{α} energy source (1485.6 eV). The spectra were collected at 3×10^{-9} Torr.

2.3. Photodetection study setup:

For the photodetection experiment, the film's edges were carefully scratched on two sides, leaving a central film area (0.25 cm^2) over the substrate. Silver paste was then applied to the two opposite edges to establish conductive contacts. The specimen was connected to a Source Measure Unit (SMU-Keithley 2450) using two probes. Photodetection measurements were carried out under ambient conditions using a bulb (9W white LED) as the light source, chosen for its broad coverage of the visible spectrum and its reduced risk of excessive local heating.



Scheme 2: Photo response study through IV and IT measurement

3. Results and Discussion

3.1. Cross-sectional image and XRD study

To verify the film thickness and bilayer structure formation, the cross-sectional FESEM images were collected from the bilayer and annealed film. Fig. 1(a) presents the bilayer images with a top layer of $\sim 150 \text{ nm}$ (Ag_2S) and a bottom layer of $\sim 450 \text{ nm}$ (In_2Se_3). Approximately the same thickness was deposited during thermal evaporation, as recorded by the thickness monitor. After annealing, the thickness remained nearly the same, as shown in Fig. 1(b). The disappearance of the distinct layer infers the formation of a single layer by annealing, through



which there is intermixing of the two layers. The different structure can be seen in the annealed film than in the as-prepared one.

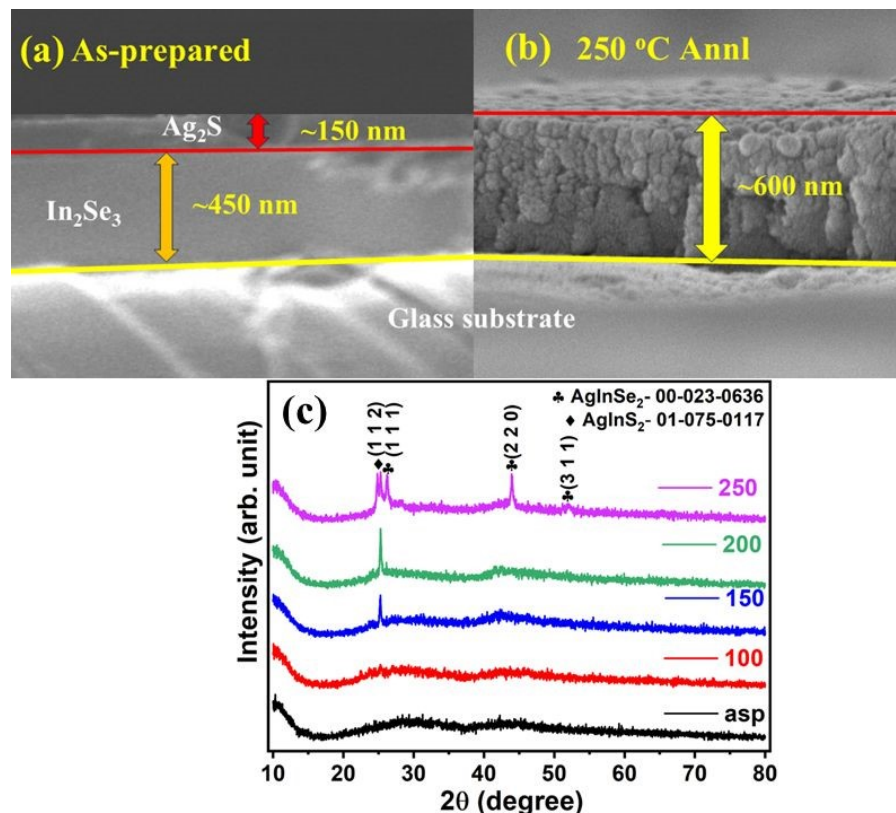


Fig. 1. Cross-sectional image of (a) as-deposited, (b) annealed film, (c) XRD pattern

XRD analysis, as depicted in Fig. 1(c), reveals a significant transformation in the structural properties of Ag₂S/In₂Se₃ thin films upon thermal annealing. The as-prepared films demonstrate an amorphous structure, lacking the long-range atomic order characteristic of crystalline materials. In contrast, the application of heat treatment promotes the development of a polycrystalline structure, indicating the formation of distinct crystalline grains within the material. This enhancement in crystallinity is directly proportional to the annealing temperature, suggesting that higher thermal energy facilitates more ordered atomic arrangements and grain growth [23]. The increased annealing temperature also encourages interdiffusion between the Ag₂S and In₂Se₃ phases, potentially leading to the formation of new or mixed phases. The XRD patterns of the annealed thin films exhibit several characteristic diffraction peaks, signifying the presence of multiple crystalline phases. Specifically, peaks observed at approximately 26.21°, 43.88°, and 51.92° are attributed to the cubic AgInSe₂ phase, correlating with the (1 1 1), (2 2 0), and (3 1 1) crystallographic planes, respectively (ICDD: 00-023-0636). Additionally, a peak detected around 25.43° corresponds to the (1 1 2) plane of the tetragonal AgInS₂ phase (ICDD: 01-075-0117). The crystallite size, denoted as D,



represents the extent of coherent diffraction within the thin films for each specific diffraction peak, essentially reflecting the grain size in a polycrystalline material. This critical structural parameter can be quantitatively determined using Scherrer's equation, which correlates the size of the crystallites to the broadening of the XRD peaks.

The crystallite size, often symbolized as D , refers to the dimensions of the coherently diffracting domains within a thin film, is expressed as,

$$\text{crystallite size } (D) = \frac{0.94\lambda}{\beta \cos\theta} \quad (1a)$$

Where Bragg's angle is θ , and the full width at half maximum (FWHM) is β . Here, $\lambda = 1.54 \text{ \AA}$ [24].

Lattice strain (ϵ) quantifies the deformation in the dimensions of a crystal lattice relative to its unstrained state. This strain can manifest in two primary forms: uniform and non-uniform strains. Uniform strain involves a consistent expansion or contraction of the unit cell across the entire crystalline volume. While uniform strain does not contribute to the broadening of diffraction peaks, it causes a shift in the peak positions and an alteration in the calculated lattice parameters [25]. This shift is a direct indicator of the average change in interplanar spacing.

The lattice strain has been calculated by using the equation [26],

$$\text{lattice strain } (\epsilon) = \frac{\beta \cot\theta}{4} \quad (1b)$$

Dislocation density (δ) is a fundamental microstructural parameter defined as the total length of dislocation lines per unit volume of a crystalline material. While dislocations are non-equilibrium defects, meaning they are not inherently stable according to thermodynamic principles, their observable density holds significant importance in influencing a material's macroscopic properties [27]. These linear crystallographic defects play a crucial role in plastic deformation, strengthening mechanisms, and various other physical phenomena in solids [28].

$$\text{Dislocation density } (\delta) = \frac{1}{D^2} \quad (1c)$$

The quantity of crystallites within a material, often denoted as the number of crystallites (N_c), is primarily governed by intrinsic structural characteristics, specifically the crystallite size (D) and the extent of agglomeration or clustering among these crystalline domains. These structural factors directly influence how many individual crystallites are present in a given volume or area of the material. A smaller average crystallite size generally implies a larger number of crystallites for a constant material volume and can be calculated as,

$$N_c = \frac{d}{D^3} \quad (1d)$$

The calculated structural parameters are summarized in Table 1. The crystallite size (D) increases progressively with annealing temperature. This enhancement can be attributed to the additional thermal energy that promotes recrystallization and re-nucleation, thereby improving the degree of crystallinity. Densification promotes the development of small nuclei during annealing, which eventually expand and unite to create bigger, more structured crystallites. As a result, numerous crystallites are generated, leading to an increased effective surface area for light absorption. This structural modification favors stronger light-matter interaction, thereby reducing the optical bandgap through enhanced absorption relative to transmission [29,30].

Table 1: Structural parameters of the $\text{Ag}_2\text{S}/\text{In}_2\text{Se}_3$ films.

Structural parameters	Asp	150 °C	150 °C	200 °C	250 °C
D (nm)	Amorphous	Amorphous	15.820	17.320	18.156
$\delta (\times 10^{15} \text{ m}^{-2})$	----	---	0.004	0.003	0.006
Lattice strain (ε)	----	-----	0.010	0.009	0.007
$N_c (\text{nm}^{-2})$	----	---	0.151	0.115	0.100

3.2. TEM Study:

TEM pictures of the prepared films at two magnifications (100 nm and 50 nm, Fig. 2(a, b)) reveal that the material consists of well-dispersed nanostructures with uniform morphology. The nanoscale features are clearly distinguished, indicating good crystallinity and homogeneity across the sample. High-resolution TEM (HRTEM) analysis, presented in Fig. 2(c), provides further insight into the structural characteristics of the material. The lattice fringes exhibit two distinct interplanar spacings: 3.39 Å, which can be assigned to the (111) plane of the AgInSe_2 phase, and 3.31 Å, corresponding to the (112) plane of AgInS_2 . The coexistence of these phases suggests a mixed chalcogenide system, where both selenium and sulfur contribute to the crystalline framework. The SAED pattern, shown in Fig. 2(d), displays a series of sharp diffraction rings, confirming the polycrystalline nature of the material. The diffraction features are in close agreement with the XRD results, thereby validating the presence of multiple crystalline phases.

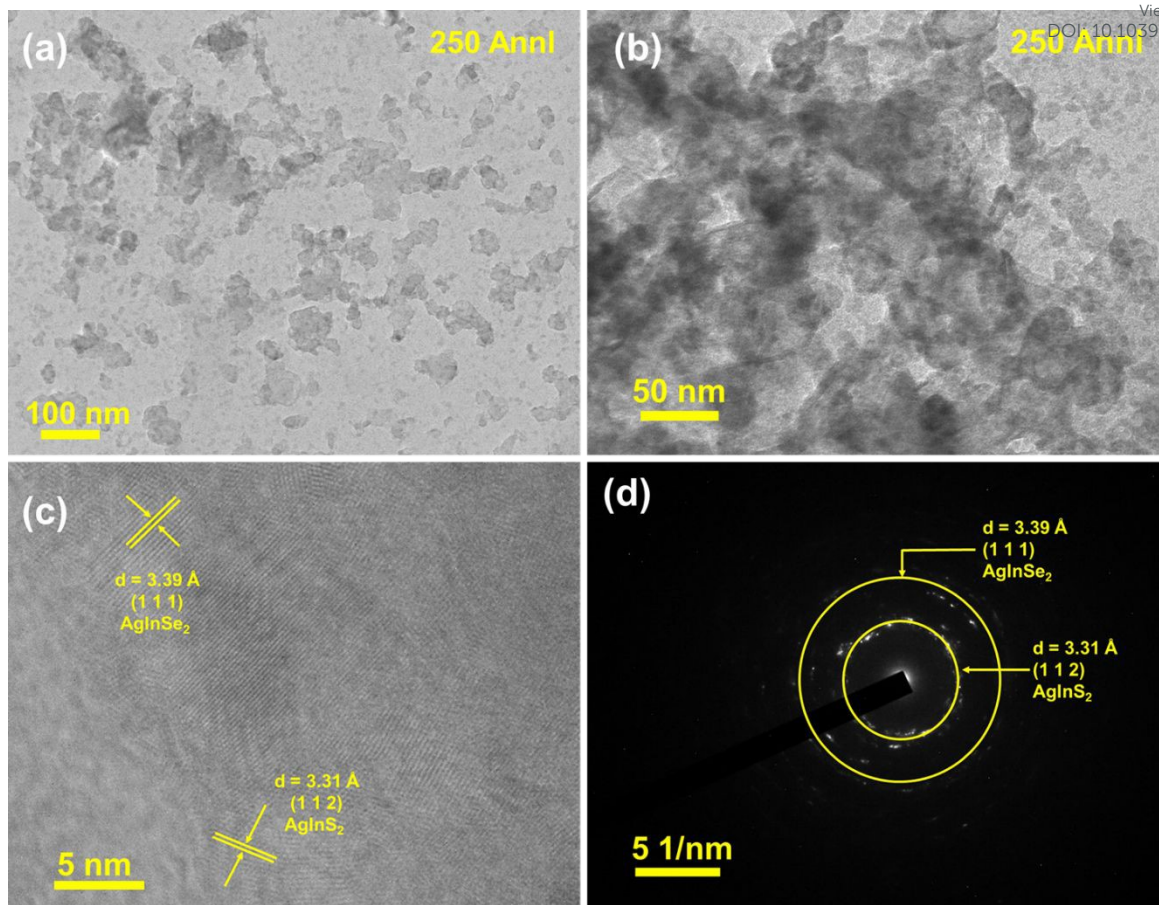


Fig. 2. TEM images at (a) 100 nm, (b) 50 nm, (c) HRTEM view, and (d) SAED pattern of 250 °C annealed $\text{Ag}_2\text{Se}/\text{In}_2\text{Se}_3$ thin film.

3.3. FESEM and EDS study

The morphology of film structure before thermal treatment and after thermal annealing is presented through the 1 μm FESEM images (Fig. 3). The as-prepared and 100 °C annealed film structures do not have as much porosity as the annealed one beyond 100 °C (Fig. 3a,b). The annealing induces porosity as seen in Fig. 3(c-e). The films consist of nanostructured particles. The degree of porosity is enhanced with the annealing conditions. The 100 nm scale film morphology shows the porosity in a better way, as presented in Fig. S1. The enhanced porosity is also seen from the TEM image (Fig. 2a, b). This increase in porosity originates from diffusion-induced phase transformation during annealing, where atomic intermixing between Ag_2S and In_2Se_3 leads to grain boundary reorganization and void formation. Such porosity enhances the active surface area, facilitating improved light absorption and faster surface charge exchange processes, which together contribute to the enhanced photodetection performance observed at higher annealing temperatures.



The existence of elements after film preparation and annealing is confirmed through EDS [View Article Online](#) [DOI: 10.1039/DNNA01136A](#)

The 250 °C annealed film shows the different elemental peaks, inferring the existence of related elements. The unassigned peaks refer to the carbon and gold peaks. Carbon tape and gold coating were used to avoid charging of the film, as the films were coated on a glass substrate. Fig. 4(a) shows the peaks for Ag, In, S, and Se, thus confirming the existence of elements in the film after annealing. The EDS pictures of the pristine and other annealed samples are depicted in Fig. S2. The elemental distribution of elements infers the uniformity of the film as illustrated in Fig. 4(b-e). The Atomic% values obtained from the EDS peaks of Ag, In, S and Se for each thin film sample shown in Table S1.

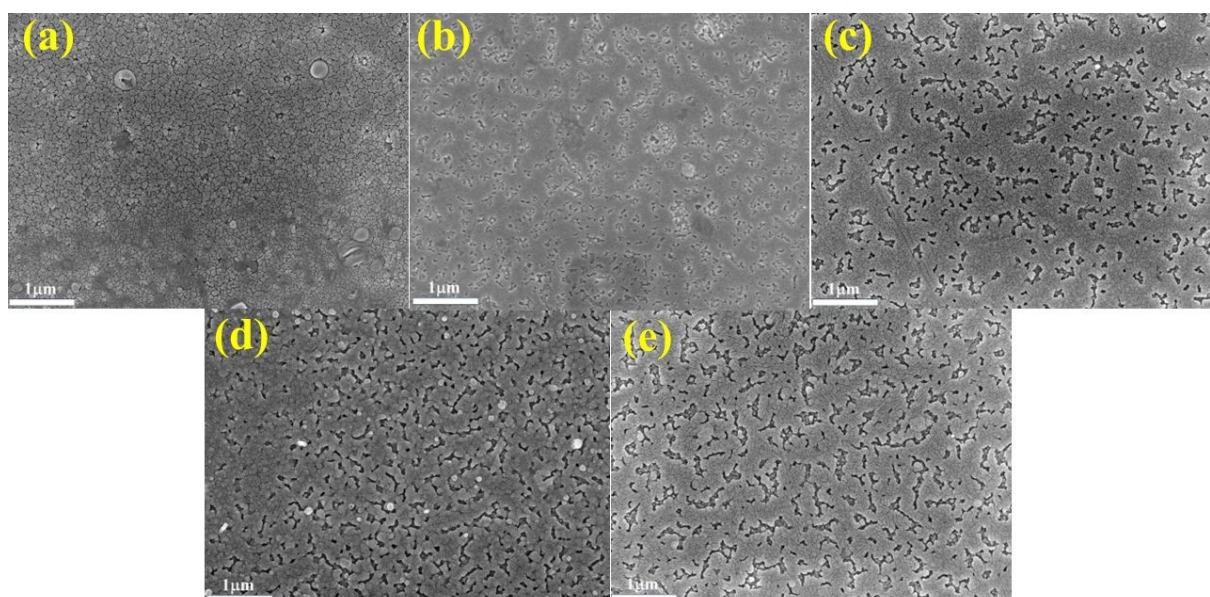


Fig. 3. FESEM view of (a) as-prepared, (b) 100 °C, (c) 150 °C, (d) 200 °C, (e) 250 °C annealed film.

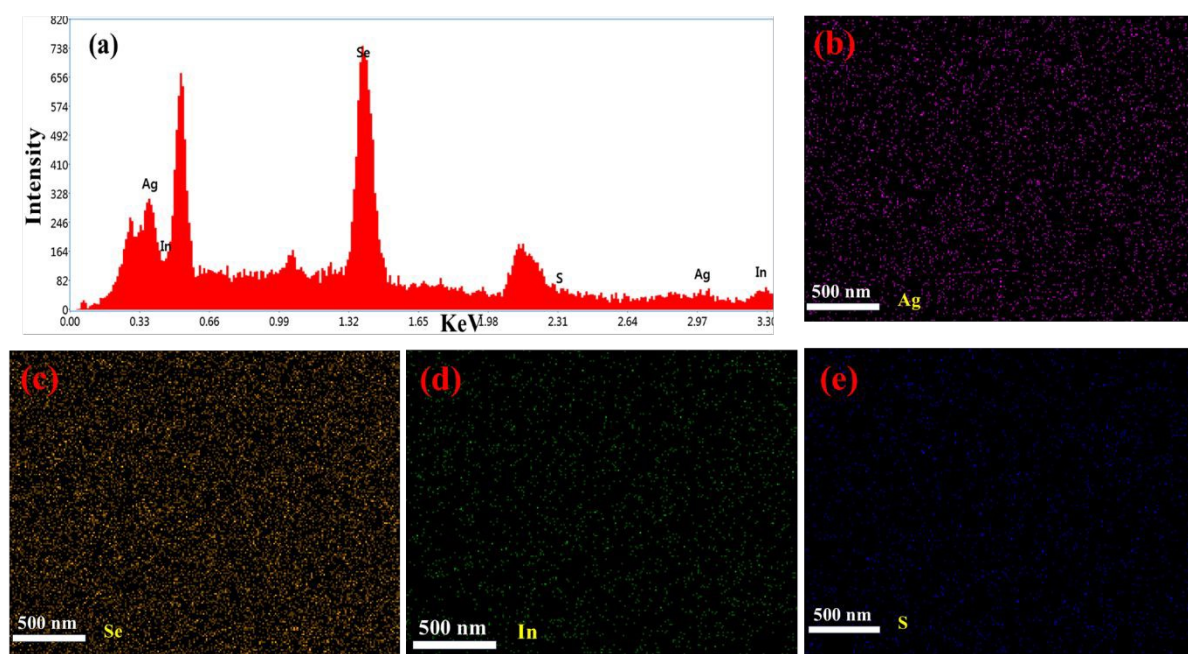


Fig. 4. (a) EDS spectra, elemental mapping of (b) Ag, (c) Se, (d) In, and (e) S in a 250 °C annealed film.

3.4. XPS Study:

XPS serves as an indispensable tool for characterizing the elemental composition of materials, particularly in the study of $\text{Ag}_2\text{S}/\text{In}_2\text{Se}_3$ films. The survey spectra of thin films annealed at 250 °C, presented in Fig. 5(a), clearly display characteristic photoelectron peaks. These peaks correspond to C 1s, In 3d, S 2p, Ag 3d, and Se 3d, providing an initial identification of the elements present within the film. A more precise understanding of the elemental states can be derived from the analysis of their respective core-level spectra.

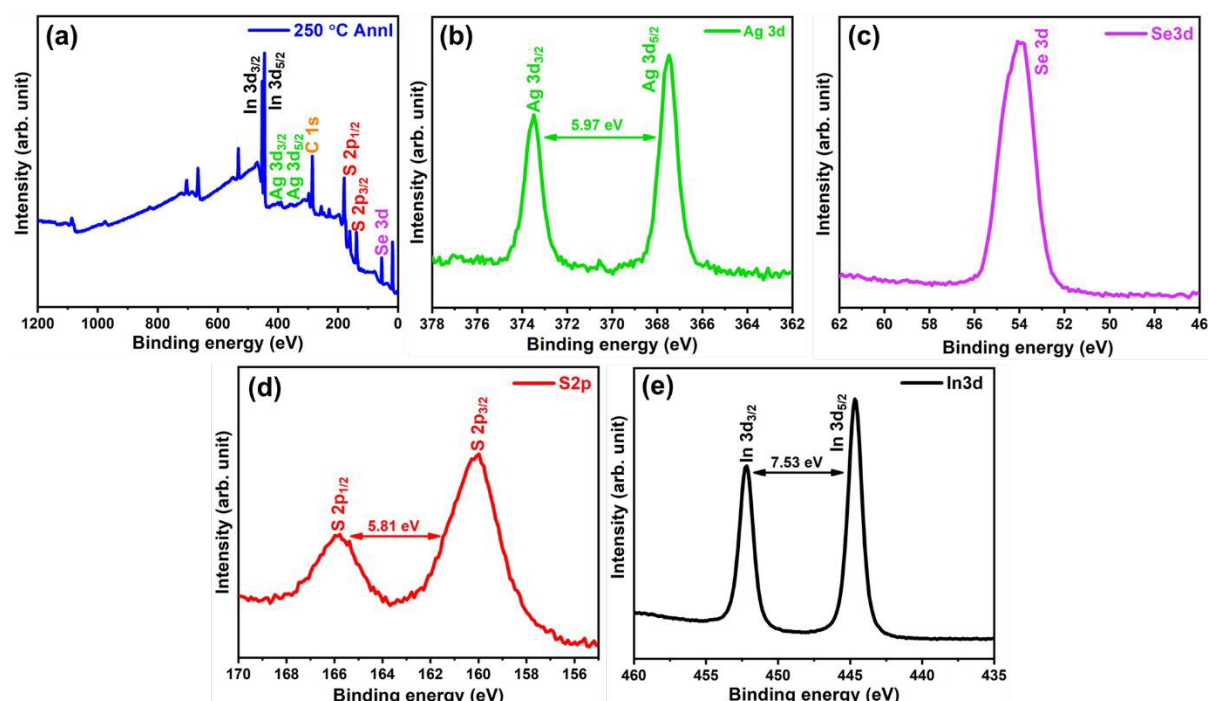


Fig. 5. XPS spectra of (a) survey spectra, (b) Ag 3d, (c) Se 3d, (d) S 2p, and (e) In 3d spectra of 250 °C annealed $\text{Ag}_2\text{S}/\text{In}_2\text{Se}_3$ thin film.

Further detailed analysis of the core-level spectra reveals specific chemical environments for each element. As depicted in Fig. 5(b), the Ag 3d core level spectrum exhibits a doublet, characteristic of spin-orbit splitting, with peaks observed at approximately 367.46 eV (Ag 3d_{5/2}) and 373.50 eV (Ag 3d_{3/2}) with a binding energy of 5.97 eV [31]. These binding energies are indicative of metallic silver (Ag (0)). Furthermore, the Se 3d peak, presented in Fig. 5(c) at around 53.95 eV, signifies the spin-orbit coupling characteristics typical for selenium in this particular thin film. Similarly, the S 2p peak, shown in Fig. 5(d), presents a doublet structure at around 160.12 eV (S 2p_{3/2}) and 165.83 eV (S 2p_{1/2}), confirming the presence of sulfur in a specific chemical state within the film and having the binding energy of 5.81 eV. Finally, the

In 3d spectrum, illustrated in Fig. 5(e), displays two distinct peaks at approximately 444.61 eV and 452.21 eV, corresponding to the In 3d_{5/2} and In 3d_{3/2} components, respectively. These values are consistent with indium in a compound form. These detailed core-level analyses collectively provide critical insights into the chemical states and bonding environments of the constituent elements in the Ag₂S/In₂Se₃ thin films [32-34].

3.5. Contact angle study

The surface wettability plays a vital role in determining the surface-related properties for different applications. The solid-liquid interface is an important aspect in applied sciences. It is evaluated based on the contact angle measurement, which provides an idea about the type of surface, whether hydrophilic or hydrophobic. The tangent (angle) of a liquid drop with a solid contact at the base determines the contact angle value (θ_c). The value of θ_c defines the nature of the surface. The angle value greater than 90° is categorized as a hydrophobic one, while the value less than 90° is regarded as a hydrophilic one [35]. The decrease in angle in hydrophilic surfaces makes the sample a super-hydrophilic one, whereas the increase in angle in hydrophobic surfaces takes it to a super-hydrophobic one. The obtained θ_c are illustrated in Fig. 6, which infers a decrease in the contact angle. This infers the decrease in hydrophobicity, which indicates the decrease in surface roughness. This suggests the water-repelling ability gradually decreased with annealing. The reason for this is the formation of pores in the annealed film with increased temperatures (FESEM image). Young's relation is used to estimate the surface energy associated with the sample by taking the surface tension of water (71.99 mN/m) [36].

$$\gamma_{se} = \frac{\gamma_w (1 + \cos \theta_c)^2}{4} \quad (2a)$$

The evaluated values in Table 2 indicate the increased surface free energy with heat treatment. The value of γ_{se} was 7.791 mN/m for the bilayer film, which increased to 12.289 mN/m after 250 °C annealing. The work of adhesion (W_{sl}) was calculated from Young–Dupré equation [37],

$$W_{sl} = \gamma_w (1 + \cos \theta) \quad (2b)$$

The W_{sl} for all the films was found to be increasing from 47.367 to 59.489 mN/m upon heat treatment (Table 2). The retention of the hydrophobic nature of the films is helpful for different applications due to their self-cleaning nature, greater chemical stability, and less degradation. For such important properties, there are potential applications in various sectors involving heat transfer applications, biomedical devices, water treatment, and so on [38]. In the context of photodetection, the gradual decrease in contact angle with annealing signifies enhanced surface

activity and oxygen adsorption–desorption capability, which directly influence carrier dynamics and photocurrent generation efficiency in $\text{Ag}_2\text{S}/\text{In}_2\text{Se}_3$ films.

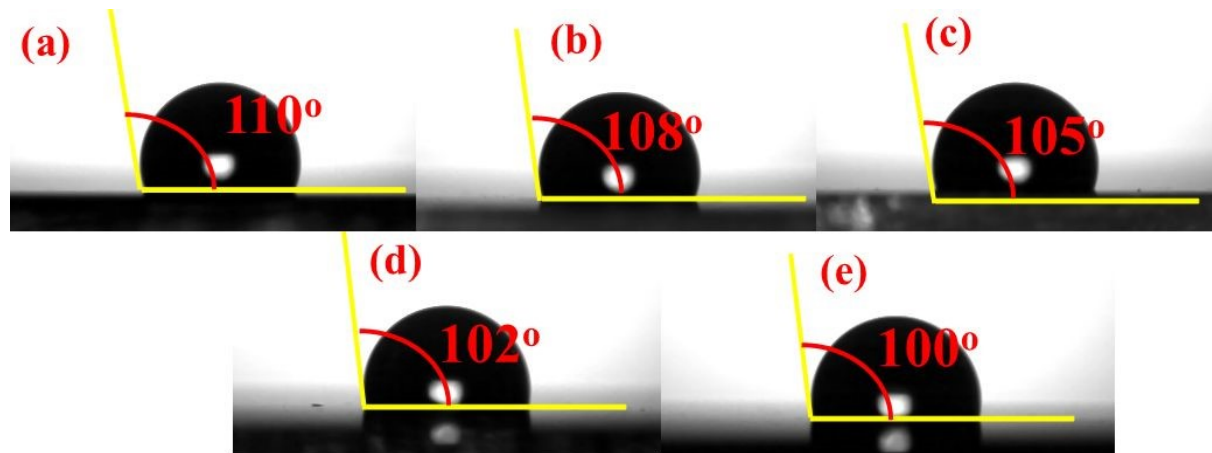


Fig.6. Contact angle images for (a) as-prepared, (b) 100 °C, (c) 150 °C, (d) 200 °C, (e) 250 °C annealed film.

Table 2. Parameters associated with contact angle

Parameters/irradiation (min)	As-prepared	100°C	150°C	200°C	250°C
θ_C (degree)	110°	108°	105°	102°	100°
γ_{se} (mN/m)	7.791	8.593	9.886	11.291	12.289
W_{sl} (mN/m)	47.367	49.743	53.357	57.022	59.489

3.6. Optical data (UV-Visible study)

The optical response of the films under study is reflected through their transmittance curve, as shown in Fig. 7(a). The systematic increase in the transmission power through annealing is well observed from Fig. 7(a). The unannealed film transmittance of ~60% is enhanced to ~95% at 1750 nm. Such increased value shows the improved transparency in the film by annealing. The appearance of wave-type fringes is the signature of uniform and homogeneous film quality [39]. The change in gap states by annealing resulted in an increased magnitude of the transmittance. The concentration of the defects, along with disorder, changed by such annealing [40]. The magnitude of transmittance is less below 1000 nm, which is favorable for solar cell applications. The higher transparency after 1000 nm wavelength range is the result of free electron interaction with the incident wave. It results in the polarization change, which is good for temperature sensors as well as IR lenses [41]. Simultaneously, the absorption edge shift to the lower wavelength side indicates the reduction in its energy gap as calculated through its absorption coefficient (α) = $\left(\frac{1}{t}\right) \ln\left(\frac{1}{T}\right)$ [42]. Here, T stands for transmittance, and 't' is the film



thickness. Fig. 7(b) infers the reduction in absorption value upon annealing. The physical quantity is essential for evaluating other necessary constants. The stability in the absorption coefficient at higher wavelengths signifies the normal dispersion behaviour.

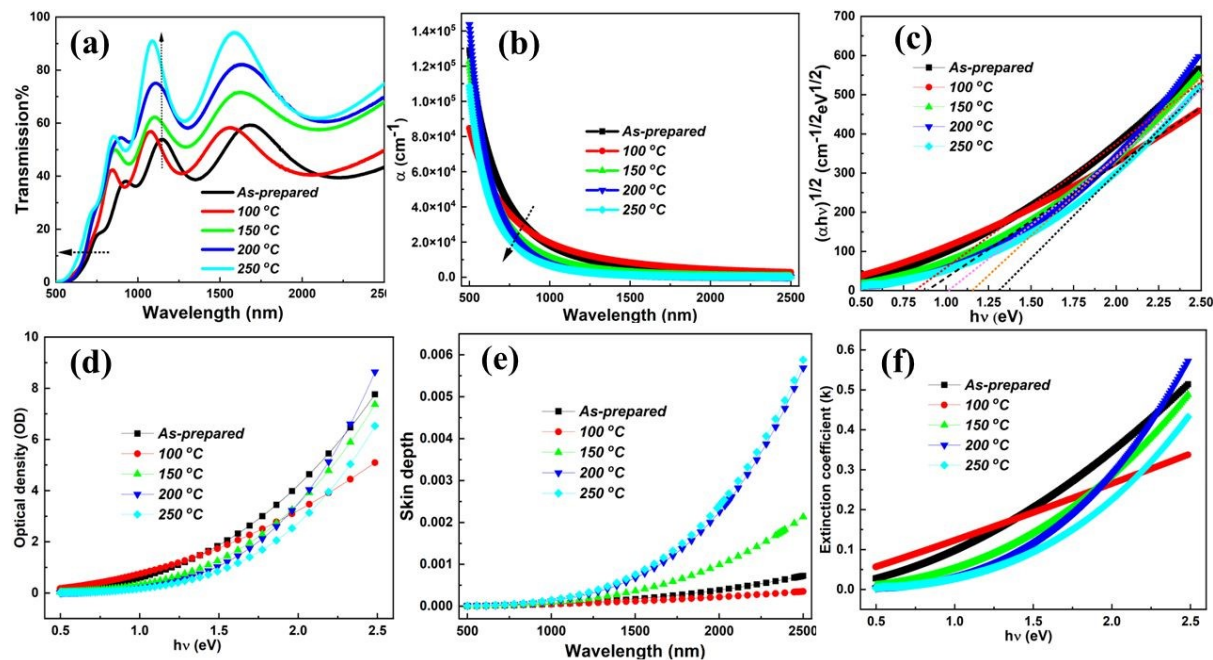


Fig. 7. (a) Transmission (b) absorption coefficient (c) bandgap (d) optical density (e)skin depth (f) extinction coefficient changes with annealing conditions.

The bandgap (E_g) depends on the value of 'α' along with the incident photon energy through the Tauc relation, [43], $(\alpha h\nu) = C(h\nu - E_g)^w$ (3)

The kind of transition between the valence and conduction bands depends on the exponent 'w' value. The direct and indirect allowed transition follows $w=1/2$ and 2. The direct and allowed forbidden transition follows $w=3/2$ and 3. The present data follows an indirect allowed transition as illustrated in Fig. 7(c). The linear fitting of the data evaluates the E_g value from its X-intercept, and the slope determines the Tauc parameter. The individual plot is illustrated in Fig. S3. The increased E_g value for the annealed film in comparison to the bilayer film shows the intermixing effects of the two layers influencing the optical bandgap [44]. The bilayer film with E_g value 0.816 eV showed an increased band gap to 1.311 eV after 250 °C annealing. Such a change is explained through Davis and Mott, the so-called "density of state model"[45]. The enhanced E_g value is because of the improved structural change by annealing. This is reflected in the XRD data. Such changes are due to the decreased disorder as measured through the Urbach energy (E_u) and Tauc constant ($B^{1/2}$). The E_u value is determined from the Urbach relation [46] $\alpha = \alpha_0 \exp\left(\frac{h\nu}{E_u}\right)$. The absorption coefficient at E_g point is represented by α_0 .

The linear fit of the absorbance data at the low absorption regime with photon energy evaluates the Eu value. From the calculation, the Eu value for the bilayer structure was found to be 543 meV, which was reduced to 432 meV for the 250 °C annealed film. The other values are mentioned in Table 3. Such reduced strength is the signature of increased structural order or decreased disorder [46]. The other parameter $B^{1/2}$ is inversely related to E_u , which shows the increased value as mentioned in Table 3 [47]. The annealing-induced saturated bond formation resulted in the reduction of defect states [48]. This implies an improvement in structure in terms of microstructural order inside the film.

Table 3. Optical parameters of the investigated $\text{Ag}_2\text{S}/\text{In}_2\text{Se}_3$ films.

Optical parameter	As-prepared	100 °C	150 °C	200 °C	250 °C
Optical band gap (eV)	0.816	0.903	1.017	1.162	1.311
Tauc parameter ($\text{cm}^{1/2}\text{eV}^{1/2}$)	243	267	298	321	344
Urbach Energy E_u (meV)	543	512	489	465	432
σ ($\times 10^{-2}$)	4.761	5.048	5.286	5.559	5.983
S_{e-p}	14.001	13.205	12.610	11.991	11.141
(η_{opt})	1.633	1.645	1.661	1.676	1.691
(ϵ_{∞})	12.852	12.117	11.303	10.445	9.715
(n_0)	3.585	3.481	3.362	3.232	3.117

The other parameters, the steepness parameter (σ) as well as electron-phonon interaction strength (S_{e-p}) and are associated with E_u [49].

$$\sigma = \frac{K_B T}{E_u} \text{ and } S_{e-p} = \frac{2}{3\sigma} \quad (4)$$

In Fig. 8(a), the increased value of σ from 4.761×10^{-2} to 5.883×10^{-2} (Table 3) suggests a steeper absorption edge with less disorder. On the other hand, S_{e-p} reduced from 14.001 to 11.141 with annealing. It refers to the weakening of electron-phonon coupling. The reduced S_{e-p} indicates the minimised lattice vibrations. It leads to an increment in lattice stability and structural order. It ultimately accounts for the improvement in optical quality with less disorder.

Optical density (OD) presents the absorption strength of the films. It is determined from the relation, $OD = \alpha \times t$. The variation in OD with 'hv' at various annealed conditions is illustrated in Fig. 7(d). Its value decreases for the annealed film at higher temperatures. The skin depth or penetration depth (δ) is another important parameter for optical quality determination. It is equal to $1/e$ times the photon density at the surface state. It is associated with semiconducting materials conductivity. The value is determined by the reciprocal of ' α ' ($\delta = 1/\alpha$) [49]. The increased skin depth with photon energy, as well as annealing temperature, results from the

View Article Online
DOI: 10.1039/DNA01136A

low absorbance, which enhances the transmittance (Fig. 7e) [42]. The extinction coefficient ($k = \frac{\alpha\lambda}{4\pi}$) measures the loss of light during crossing through the sample by scattering and absorption. The change in k various annealing states is presented in Fig. 7(f). It presents a lower value for the annealed film over the as-prepared bilayer film. The 'k' values increased with photon energy and decreased with annealing temperature.

These optical property trends with annealing confirm that the improvement in transparency, bandgap, and optical constants arises from enhanced crystallinity, reduced defect states, and the formation of well-ordered $\text{AgInS}_2/\text{AgInSe}_2$ phases, all of which play a crucial role in optimizing the light absorption and charge transport behavior of the thin film photodetector.

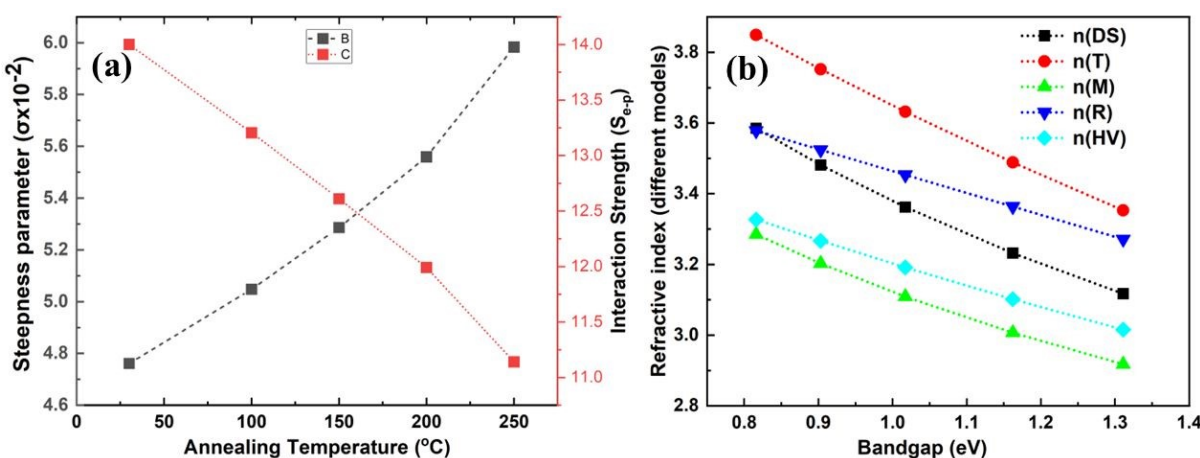


Fig. 8. (a) Variation of Se-p and 'σ' with annealing temperature (b) Refractive index at different bandgap values through various models.

The high-frequency dielectric parameter is evaluated by $\epsilon_L = n^2$. In the present study, ϵ_L increased with irradiation time (Table 3). It is attributed to the electrical polarizability of the material and is connected with free charge carriers affecting polarization [50]. The optical conductivity (η_{opt}) is determined by, $\eta_{opt} = \left(\frac{c}{n_0}\right)^{1/4}$, with $c = 25.54$ and are given in Table 3 [50]. It measures the affinity of an atom for bond formation. In the present case, it increased from 1.633 (un-annealed) to 1.691 for 250°C annealed film (Table 3).

The refractive index (n) evaluates the dispersion of light waves and other nonlinear optical phenomena. The calculation of 'n' from E_g by using the Dimitrov and Sakka empirical relation establishes a useful connection between the electronic band state and the optical dispersion of the films [52]

$$\frac{n^2 - 1}{n^2 + 2} = 1 - \sqrt{\frac{E_g}{20}} \quad (5a)$$

With increasing annealing temperature, the refractive index (n) exhibited a notable decrement (Table 3 and Fig. 7(b)). In the present study, n values were found to vary between 3.58 and 3.11, suggesting their suitability for applications in integrated photonic devices, ultrafast optical modulators, infrared (IR) sensors, and related optoelectronic systems [53]. The opposite variation of " E_g " with " n " follows

$$\text{Moss's rule, i.e., } E_g n^4 \sim \text{constant} \quad [54]. \quad \text{The } E_g n^4 \sim \text{constant leads to as, } n_M = \sqrt[4]{\frac{95}{E_g}}, \quad (5b)$$

with ' k ' = 95 eV. The rectified Ravindra's formula $n_R = 4.084 [0.62 \times E_g]$ is used [55] for the evaluation of ' n ' below 4 eV materials. Likewise, for low E_g films, Herve-Vandamme [56] relation is used, which is in accordance with oscillator theory, expressed as, $n^2 = 1 + \left(\frac{A}{E_g + B}\right)^2$. (5c)

With, $A \approx 13.6 \text{ eV}$, (~hydrogen ionisation energy), and $B = 3.4 \text{ eV}$. Considering these values, the above relation becomes, $n_{[HV]} = \sqrt{1 + \left(\frac{13.6}{E_g + 3.47}\right)^2}$. (5d)

The exponential relation of ' n ' for semiconductors with band gaps is given by Tripathy [57], the relation, $n_T = 1.73 \times [1 + 1.9017 \times e^{-0.539 \times E_g}]$ (5e)

The values obtained from different models are expressed in Fig. 8(b). It presents the inverse relation with E_g .

3.7. Photo response study

The I-V features for all films under illuminated and dark states are illustrated in Fig. 9(f, g), while Fig. S4 presents corresponding plots with a linear Y-axis. These curves exhibit clear symmetry for each thin film, with the photocurrent consistently surpassing the dark current, indicating effective light-induced charge separation and material interaction. [58] From the linear plotting in Fig. S4, the peak current values under light (I_L) and dark (I_D) states were extracted and illustrated in Table 4. The photosensitivity of each film was calculated by the formula in equation (6a). All thin films displayed significant photosensitivity, with the sample annealed at 250°C exhibiting the highest photodetection capability. This enhancement is linked to improved crystallinity at higher annealing temperatures, which boosts photoresponsivity and detectivity. [59]

Photodetector performance under various light intensities is basically driven by the formation of electron-hole pairs proportional to the power of incident light. Incorporating an Ag_2S layer on In_2Se_3 increases carrier concentration in the In_2Se_3 , enhancing the overall response. Additionally, surface interactions involving oxygen play a critical role: in the dark, oxygen molecules adsorb onto the surface, capturing electrons ($\text{O}_2 + e^- \rightarrow \text{O}_2^-$), while under illumination, photogenerated holes trigger desorption of oxygen, freeing electrons to conduction band and elevating photocurrent [23]. Key performance indicators such as

photoresponsivity (R) and detectivity (D) were calculated by standard formulas and are also detailed in Table 4[1,60-62]

$$\text{Photo Sensitivity} = \frac{I_L - I_D}{I_L} \times 100\% \quad (6a)$$

$$\text{Responsivity (R)} = \frac{I_L}{A \times P_{in}} \quad (6b)$$

$$\text{Detectivity (D*)} = R \sqrt{\frac{A}{2eI_D}} \quad (6c)$$

Here, A = Active surface area = 0.25 cm²,

P_{in} = Incident light's power density = 20 mWcm⁻²,

$e = 1.602 \times 10^{-19}$ C = electronic charge

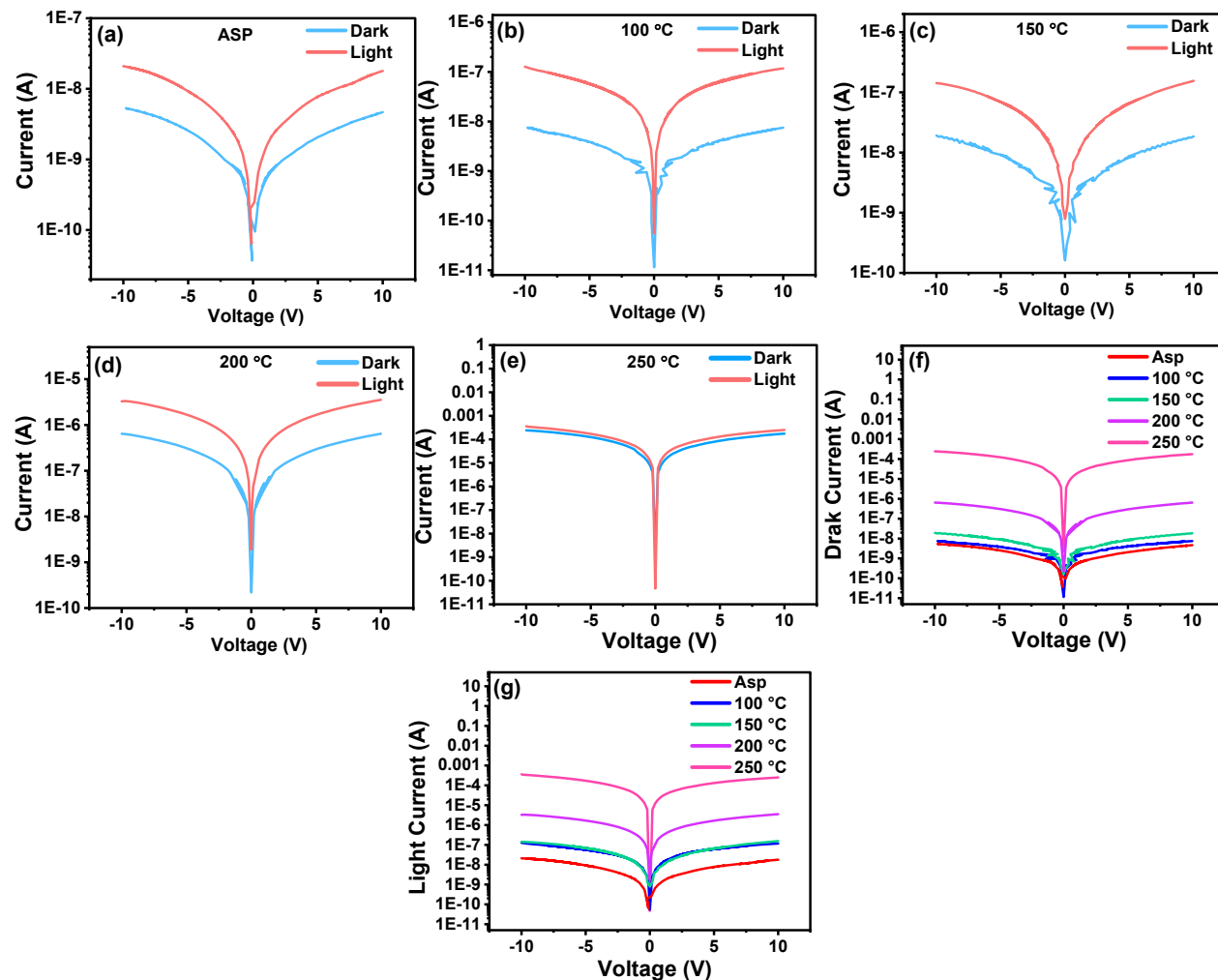


Fig. 9. The current–voltage (I–V) characteristics of $\text{Ag}_2\text{S}/\text{In}_2\text{Se}_3$ thin films, presented on a logarithmic scale under both dark and illuminated conditions. Individual plots are displayed for (a) the as-prepared sample, and those annealed at (b) 100°C, (c) 150°C, (d) 200°C, and (e) 250°C. Additionally, combined I–V curves for all samples are provided under (f) dark and (g) light conditions.



Table 4. The figure of merit of all the as-prepared and annealed $\text{Ag}_2\text{S}/\text{In}_2\text{Se}_3$ thin films.

Sample	I_L (A)	I_D (A)	$I_L - I_D$ (A)	Photo sensitivity (%)	Responsivity (R) (AW ⁻¹)	Detectivity (D*) (Jones)
Asp	1.79×10^{-8}	4.66×10^{-9}	1.32×10^{-8}	73.96	3.58×10^{-6}	3.09×10^8
100°C	1.17×10^{-7}	7.5×10^{-9}	1.09×10^{-7}	93.61	2.34×10^{-5}	2.89×10^7
150°C	1.55×10^{-7}	1.85×10^{-8}	1.36×10^{-7}	88.06	3.10×10^{-5}	1.95×10^8
200°C	3.53×10^{-6}	6.42×10^{-7}	2.89×10^{-6}	81.84	7.07×10^{-4}	7.32×10^9
250°C	2.51×10^{-4}	1.75×10^{-4}	7.66×10^{-5}	30.43	5.03×10^{-2}	1.44×10^7

The I-V characteristics of $\text{Ag}_2\text{S}/\text{In}_2\text{Se}_3$ thin films, under both dark and illuminated states, demonstrate clear symmetry and a consistent increase in current under illumination across all samples. The logarithmic plots (Fig. 9a–e) show enhanced photocurrent (I_L) compared to dark current (I_D), with the 250°C annealed sample exhibiting the highest absolute current levels. However, Fig. S4 (with a linear y-axis) reveals that while the 250°C sample produces the highest I_L and I_D values, the contrast between light and dark currents, indicative of sensitivity, is reduced compared to other annealed conditions. Quantitative analysis from Table 4 supports this observation. The highest photosensitivity (93.61%) is recorded for the 100°C sample, followed closely by the 150°C and 200°C samples. The 250°C sample, despite showing the largest I_L (2.51×10^{-4} A), demonstrates the lowest relative photosensitivity (30.43%) due to a high baseline dark current. Nevertheless, its responsivity (5.03×10^{-2} A/W) and detectivity (1.44×10^7 Jones) remain significant, highlighting its utility in applications requiring high absolute photocurrent rather than contrast.

Overall, moderate annealing temperatures (100–250°C) improve photodetection performance by optimizing light-induced carrier generation and suppressing dark current. The 200°C sample strikes a balance, offering enhanced current response, high responsivity (7.07×10^{-4} A/W), and the best detectivity (7.32×10^9 Jones), attributed to improved crystallinity and reduced surface recombination.

A comparative analysis of the films annealed at different temperatures reveals that the photoresponsivity (R) correlates strongly with the films' structural and optical properties. As the annealing temperature increases from 100 °C to 200 °C, enhanced crystallinity, improved interfacial uniformity, and reduced defect density collectively enhance carrier mobility and light absorption, leading to higher R and D values. However, further annealing to 250 °C introduces excess charge carriers and defect-assisted conduction pathways, increasing dark current and reducing photosensitivity. Thus, the 200 °C annealed film achieves the optimal

balance between crystallinity, defect control, and interfacial quality, resulting in the highest responsivity and detectivity among all samples.

View Article Online
DOI: 10.1039/DNA01136A

However, the rise in dark current at 250 °C indicates that excessive annealing increases carrier concentration and defect-assisted conduction, thereby reducing photosensitivity. This demonstrates that optimal photodetector performance arises not from maximum current output but from a balanced combination of crystallinity, defect density, and interfacial integrity conditions best achieved at 200 °C. Table S2 compares the key photodetection parameters of the present $\text{Ag}_2\text{S}/\text{In}_2\text{Se}_3$ device with other 2D/ In_2Se_3 -based systems reported in the literature. The results demonstrate that the optimized $\text{Ag}_2\text{S}/\text{In}_2\text{Se}_3$ heterostructure exhibits comparable responsivity and detectivity, while offering a broader visible spectral response due to efficient interfacial charge transfer and reduced recombination losses.

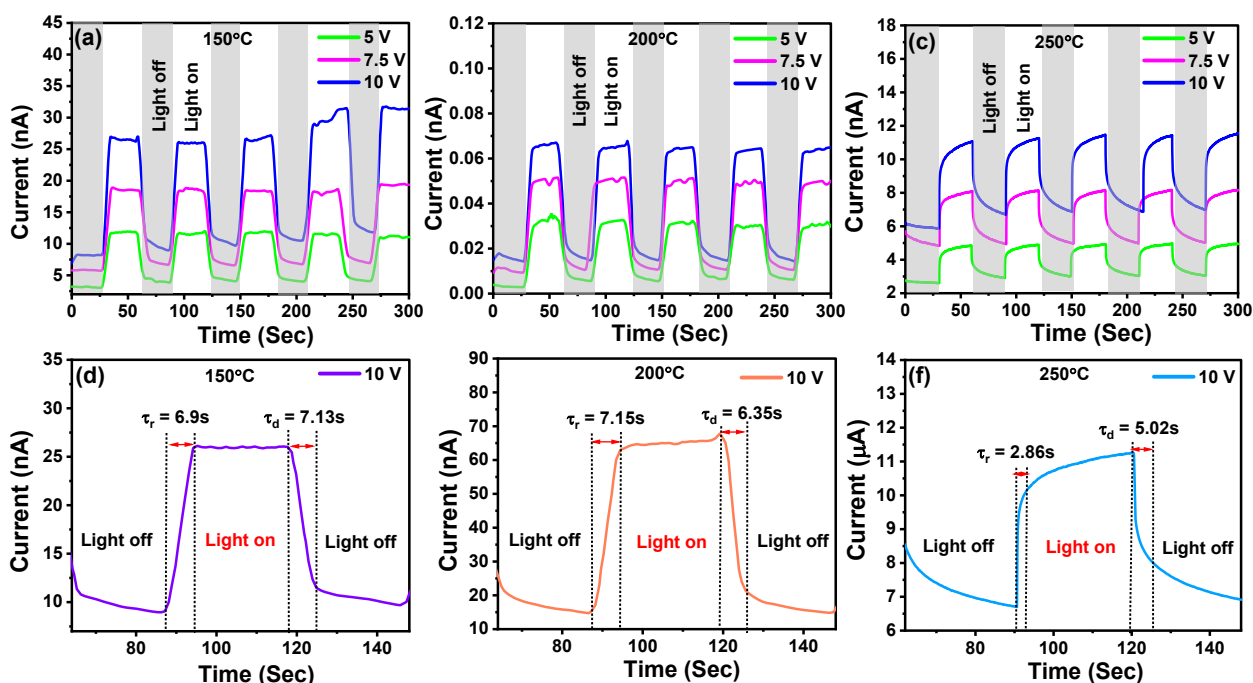


Fig. 10. Temporal photoresponse curves illustrating the change in current over time at bias voltages of 5, 7.5, and 10 V for annealed thin films at (a) 150°C, (b) 200°C, and (c) 250°C. The rise and fall times of the photocurrent within a selected time interval are shown for the films annealed at (d) 150°C, (e) 200°C, and (f) 250°C, respectively.

Fig. 10(a-c) displays I-T curves for $\text{Ag}_2\text{S}/\text{In}_2\text{Se}_3$ films annealed at 150°C, 200°C, and 250°C under bias voltages of 5, 7.5, and 10 V, showing distinct on/off light cycles. All samples exhibit a sharp increase in current upon illumination, followed by a quick drop when the light is off, driven by enhanced carrier drift velocity. The increased photocurrent with higher bias voltages is attributed to stronger electric fields, which improve charge separation, reduce recombination,

and expand the depletion region, leading to more efficient carrier generation and collection. Variations in maximum current among samples are likely influenced by defect states. After the light is off, the photocurrent decreased due to recombination between trapped and free carriers, with additional effects from non-radiative processes and carrier transport variations. For consistent analysis, a specific peak within the 60-150 second interval is selected for all samples Fig. 10(d-f). From this peak, key parameters such as light-on (I_{on}), light-off (I_{off}), and I_{on}/I_{off} ratios during rise and decay phases are extracted and presented in Table 2 to evaluate photodetector performance.

Furthermore, the transient photoresponse (I-T) curves in Fig. 10(a-c) show that the photocurrent quickly returns to its baseline after each illumination cycle, indicating the absence of persistent photoconductivity. This behavior reflects efficient carrier recombination and minimal trap-assisted retention, confirming the fast and reversible photoresponse characteristics of the $\text{Ag}_2\text{S}/\text{In}_2\text{Se}_3$ heterostructure.

Table 5. Photodetector parameters of the $\text{Ag}_2\text{S}/\text{In}_2\text{Se}_3$ thin films for both rise and decay conditions.

Sample	During Rise				During Decay			
	I_{on} (nA)	I_{off} (nA)	I_{on}/I_{off}	τ_r (s)	I_{on} (nA)	I_{off} (nA)	I_{on}/I_{off}	τ_d (s)
150°C	25.88	9.08	2.85	6.9	25.92	11.26	2.3	7.13
200°C	62.35	15.72	3.96	7.15	67.74	21.25	3.18	6.35
250°C	10.14	6.71	1.51	2.86	11.24	8	1.4	5.02

Rise time (τ_r) and decay time (τ_d) are essential indicators of a photodetector's responsiveness. The rise time measures how quickly the current increases (from 10% to 90%) when light is applied, while the decay time reflects how fast it returns to baseline (from 90% to 10%) after light is removed. Shorter τ_r and τ_d values indicate faster response and recovery, which are critical for high-speed light detection. [5] These parameters, extracted from Fig. 10(d-f), are presented in Table 5 to evaluate the dynamic performance of the $\text{Ag}_2\text{S}/\text{In}_2\text{Se}_3$ photodetectors.

Fig. 10 and Table 5 present the temporal photo response behavior of $\text{Ag}_2\text{S}/\text{In}_2\text{Se}_3$ films annealed at 150°C, 200°C, and 250°C under different bias voltages (5, 7.5, and 10 V). All samples show a repetitive and reversible change in current upon cyclic illumination, indicating stable photodetector operation. The response amplitude increases with higher bias voltage, especially evident in the 200°C sample (Fig. 10b), which exhibits the highest photocurrent. The

extracted photodetector parameters (Table 5) reveal that the 200°C sample demonstrates the most favourable characteristics overall. It shows the highest photocurrent during both the rise (62.35 nA) and decay (67.74 nA) phases, coupled with a strong I_{on}/I_{off} ratio of 3.96 (rise) and 3.18 (decay). Its rise and fall times ($\tau_r = 7.15$ s, $\tau_d = 6.35$ s) are moderate and well-balanced, suggesting efficient charge separation and recombination kinetics. The optimal dynamic behavior at 200 °C arises from a well-balanced microstructure where enhanced crystallinity and controlled interdiffusion reduce trap-assisted recombination, thereby enabling faster carrier transport and recovery compared to under or over-annealed films.

Fig. S5 illustrates the current–time (I-T) stability behavior of $\text{Ag}_2\text{S}/\text{In}_2\text{Se}_3$ thin films annealed at 150 °C, 200 °C, and 250 °C under continuous illumination for 1 hour (3600 sec.). All three samples exhibit a steady photocurrent response with minimal fluctuation, confirming good temporal stability. The photocurrent initially increases slightly before reaching saturation, which can be attributed to the gradual stabilization of charge trapping and de-trapping processes at the film–electrode interface. The 200 °C annealed sample shows the most stable and consistent current output, with negligible drift over time, indicating robust charge transport and minimal defect-mediated recombination. In contrast, the 250 °C film exhibits higher absolute current but with a slow saturation trend due to increased defect density. Overall, the I-T stability analysis confirms that the $\text{Ag}_2\text{S}/\text{In}_2\text{Se}_3$ heterostructures maintain stable photocurrent characteristics over prolonged operation, particularly for the optimally annealed 200 °C sample.

In contrast, the 250°C sample exhibits the fastest response ($\tau_r = 2.86$ s) and decay ($\tau_d = 5.02$ s) but suffers from reduced current contrast ($I_{on}/I_{off} \approx 1.5$), indicating lower sensitivity. Meanwhile, the 150°C sample shows a moderate current level and contrasts with longer response times ($\tau_r = 6.9$ s, $\tau_d = 7.13$ s), suggesting slower carrier dynamics. Overall, the 200°C annealed film stands out as the optimal candidate, combining high photocurrent, strong on/off contrast, and reasonable response times, ideal attributes for practical photodetector applications. Although wavelength-dependent photoresponse measurements could not be performed due to the unavailability of a monochromatic light source, the use of a broad-spectrum white LED ensures uniform excitation across the visible region. The strong absorption and rapid transient response observed confirm the film's potential for broadband visible photodetection. Future work will include detailed spectral responsivity analysis using tunable light sources.

4. Computational Study

The structural stability, electronic structure, and optical behavior of the heterostructure layer

of Ag_2S and In_2Se_3 with different proportions (1:3 and a single layer of Ag-S-Se-In) have been calculated by the full potential linearized augmented plane wave (FP-LAPW) within the framework of DFT through MedeAVASP package [63,64]. DFT was used to obtain an understanding of atomistic-scale interactions in determining the various physical properties of a material. The heterostructures were constructed along the (1 0 0) plane of Ag_2S and the (2 -1 0) of the In_2Se_3 with 15 Å of vacuum region given along the z-direction by using VESTA visualisation software [65]. The correlation and exchange energies were evaluated within GGA by Perdew-Burke-Ernzerhof (PBE) parametrization [66]. Finally, the Hubbard correction value, $U_d=4$ for Ag and $U_p=10$ for In, Se, and S atoms, was added to enhance the localization and short-range interactions. The self-consistent calculations were performed with a self-consistent field (SCF) energy convergence threshold of 10^{-6} eV and a planewave cutoff of 258.689 eV. The Brillouin zone was integrated with a 2x2x1 Monkhorst-Pack grid, and the Gaussian scheme with a broadening of 0.003 Ry was used in calculation. The band structure was calculated along F- Γ -B-G- Γ high symmetry directions, and the corresponding density of states is depicted in Fig. 11(a-c). The conduction band is dominated by Se-4p, In-5s atoms in a 1:3 layer, but in the 1:1 case, mostly by Se-4p atoms, and the valence band is occupied by Se-4p, S-3p in a 1:3 layer, whereas in a 1:1 layer, it is occupied by Se-4p near the Fermi level. This indicates that stronger interaction or bonding is more likely in Se, In, and S atoms. The band gap (E_g) for a 1:3 proportion heterostructure layer of Ag_2S and In_2Se_3 is 0.78987 eV, whereas for a single layer of Ag-S-Se-In is 1.37339 eV. The contour plot of electron charge density shows that more charge is accumulated around the Se atom in both these cases, which shows that the Se atom plays a crucial role in the materials' properties [Fig. 12]. A similar simulation was implemented for the optical parameter calculations, such as real and imaginary parts of dielectric constant, real and imaginary parts of conductivity, reflectivity, refractive index, attenuation coefficient, extinction coefficient, and absorption, respectively, within 0-20 eV photon energy.

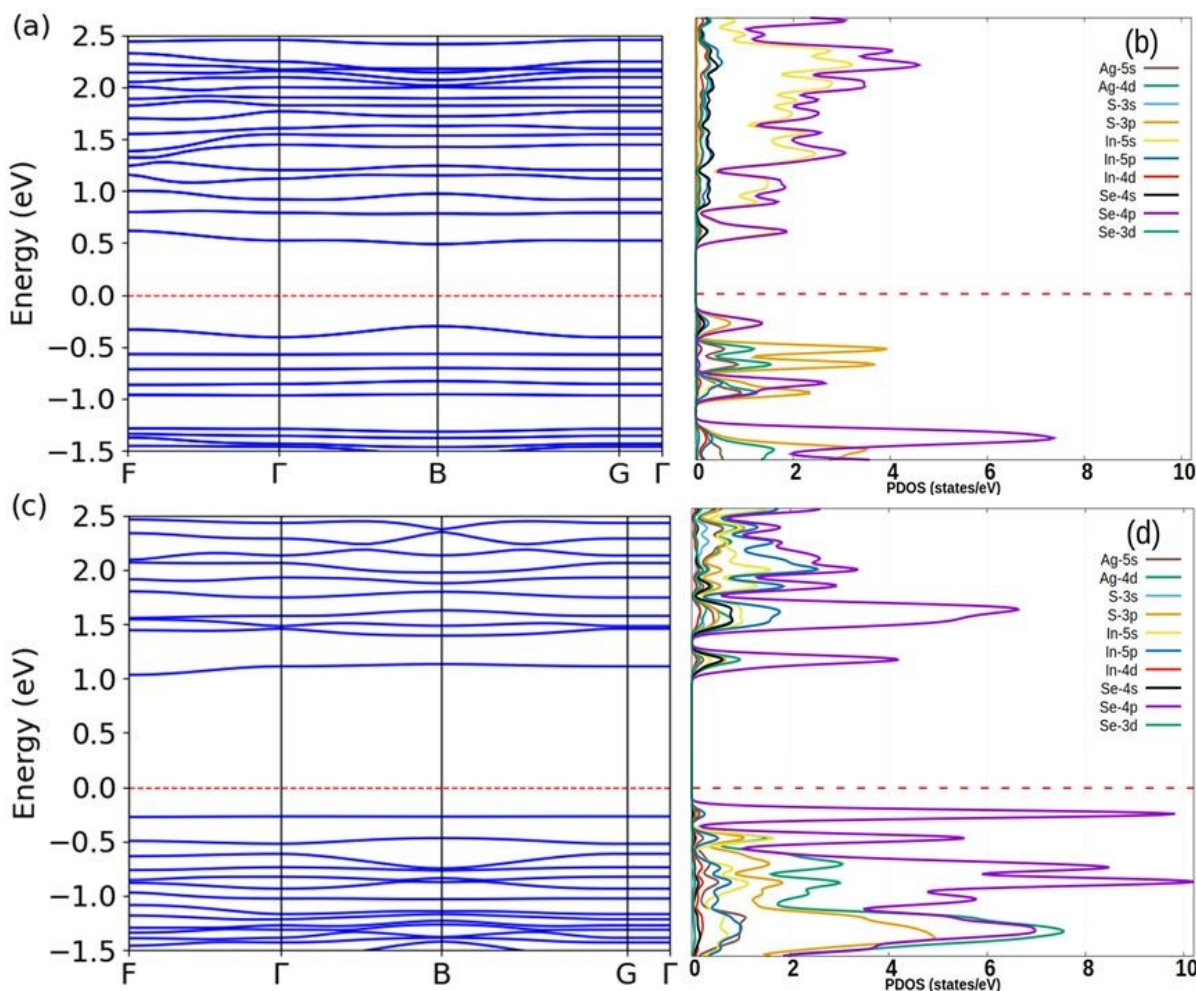


Fig. 11. Calculated band structures and corresponding density of state of (a,b) 1:3 proportion layer of Ag_2S and In_2Se_3 heterostructure (c,d) single layer of Ag-S-Se-In.

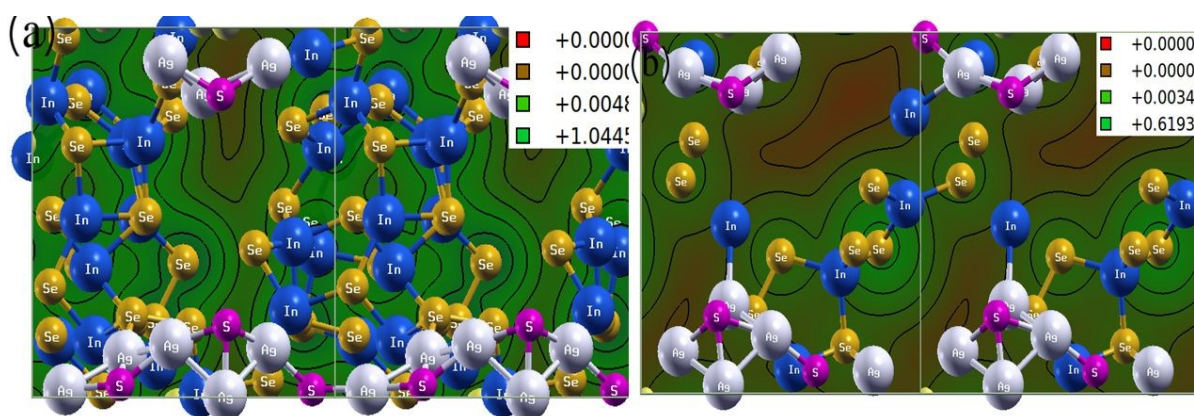


Fig. 12. Contour plot for the charge density of (a) 1:3 proportion layer of Ag_2S and In_2Se_3 heterostructure and (b) single layer of Ag-S-Se-In.



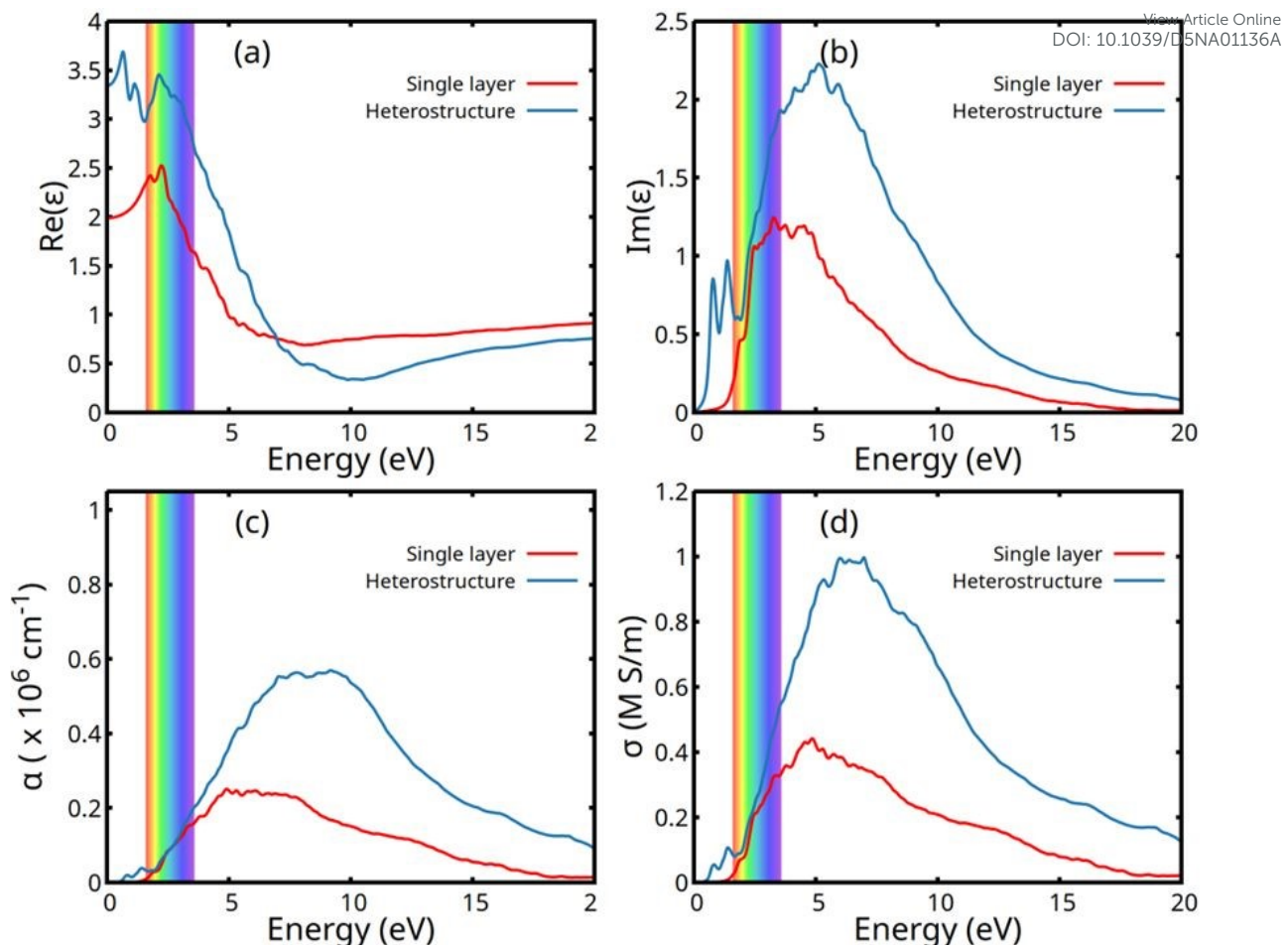


Fig. 13. Ag₂S and In₂Se₃ heterostructure 1:3 and 1:1 proportion (a) real part, (b) imaginary part of dielectric function, (c) absorption coefficient, (d) optical conductivity.

The optical parameters of a material are crucial to investigate an excellent candidate for photovoltaic and optoelectronic applications. When the matter interacts with the electromagnetic radiation, it gets polarized by the applied electric field. It affects its interaction with electromagnetic waves. Fig. 13(a, b) illustrates the real and imaginary parts of the dielectric parameter. The imaginary component, indicating the material's absorption of electromagnetic radiation, denotes the energy loss per unit volume. This aspect is directly linked to electronic transitions between unoccupied and occupied states within the sample. The real part presents peaks \sim 1.13 eV and 1.78 eV for hetero and single layers of Ag-S-Se-In, respectively. Then it decreased with increased photon energy. Within the zero-frequency range, the static dielectric constant for the heterolayer is 3.34, whereas for a single layer, it is 1.98. Fig. 13(c) depicts the maximum absorption coefficient values at photon energy of 9.1 eV for hetero and 4.8 eV for a single layer of Ag-S-Se-In.



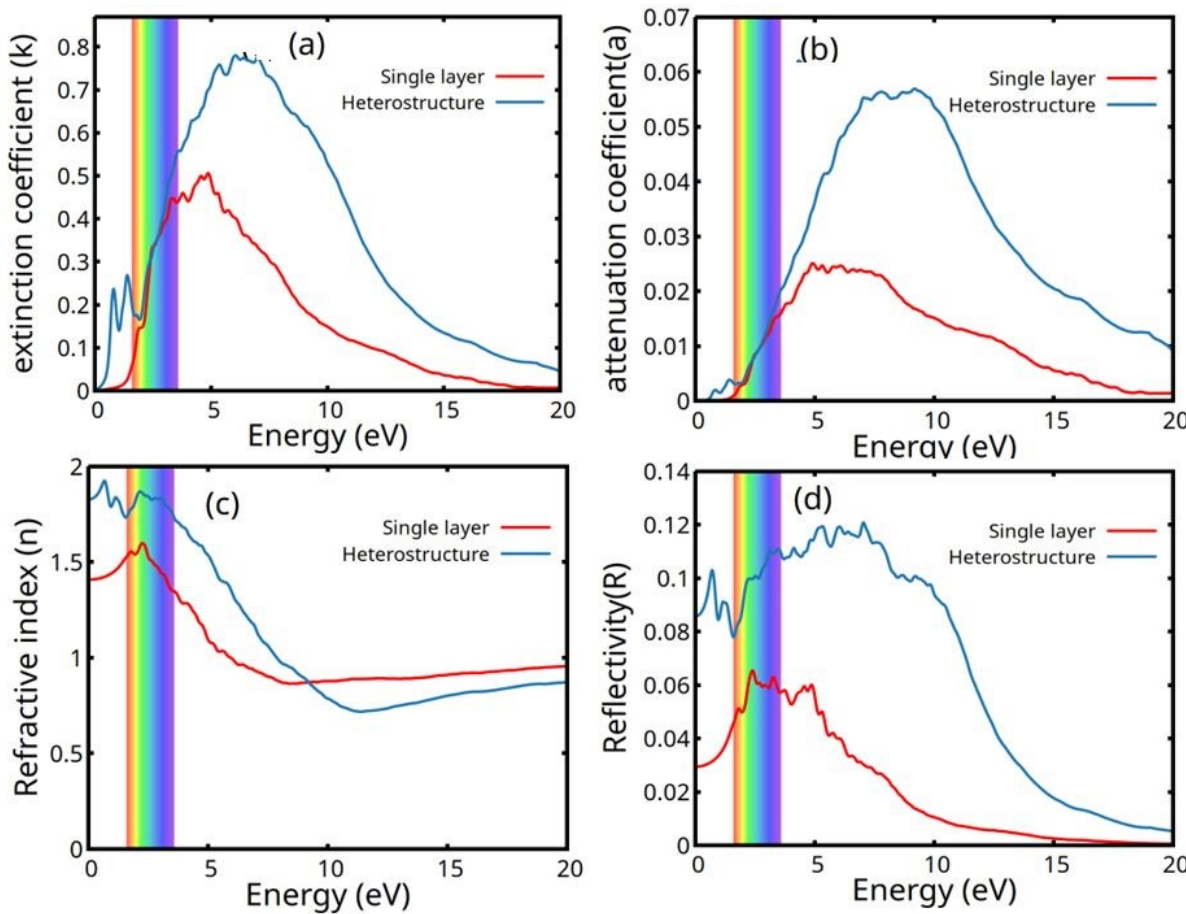


Fig. 14. Ag_2S and In_2Se_3 heterostructure 1:3 and 1:1 proportion (a) extinction coefficient, (b) attenuation coefficient (c) refractive index, (d) reflectivity.

Optical conductivity, extinction coefficient, attenuation coefficient, and refractive index are displayed in Fig. 14(a-d) for both the hetero layer and the single layer of Ag-S-Se-In. Fig 14(d) indicates around 8% of reflectance for heterolayer and 3% of reflectance for single layer at 0 eV.

It should be noted that the computational model represents an atomically thin Ag-S-In-Se heterostructure, designed to approximate the local interfacial environment between Ag_2S and In_2Se_3 layers. This simplified configuration allows accurate insight into charge transfer, electronic coupling, and band alignment at the junction, which govern the experimentally observed optoelectronic behavior, even though it does not replicate the full experimental film thickness.



5. Conclusion

The diffusion of Ag_2S into In_2Se_3 heterostructure-based films was studied for a Visible light photodetector. The annealing resulted an increased photo detectivity of 7.32×10^9 Jones for 200 °C annealed film. The intermixing of the layers resulted in the transformation of amorphous to crystalline phase and enhanced the photo current during both the rise (62.35 nA) and decay (67.74 nA) phases. The strong $I_{\text{on}}/I_{\text{off}}$ ratio of 3.96 (rise) and 3.18 (decay) was observed, resulting in its rise and fall times as $\tau_r = 7.15\text{s}$, and $\tau_d = 6.35\text{s}$. These are moderate and well-balanced, suggesting efficient charge separation and recombination kinetics suitable for visible light photodetection. The crystallinity increase is reflected by the increase in the crystallinity size from 15.820 nm to 18.156 nm upon annealing. The developed AgInSe_2 and AgInS_2 phases resulted from the intermixing, which reduced the disorder, as well as being well visualised from SAED and HRTEM images. The increase in porosity in the films, as noticed from FESEM morphology, resulted in a decrease in hydrophobicity. The contact angle decreased from 110 ° to 100 ° upon 250 °C annealing. The increased transmittance is accompanied by reduced optical density with enhanced skin depth. The optical gap increased from 0.816 to 1.311 eV upon 250 °C annealing, which is well supported by the DFT study. The steepness parameter increased from 4.761×10^{-2} to 5.983×10^{-2} , resulting from the decreased Urbach energy from 543 meV to 432 meV upon annealing. The decreased refractive index and extinction coefficient is well supported by the DFT result. The overall optical and photo response behaviours of the films suggest their wider application as Visible light photodetectors and are useful for various optoelectronic devices.

Supporting Information

FESEM images at 100 nm scale for all films, EDS spectra, individual bandgap plot and IV data for dark and light current of all the films.

Conflicts of interest

There are no conflicts to declare.

Data Availability Statement

All the data related to the present work are included in the manuscript and supporting information and will be available upon reasonable request.

Acknowledgments

The author, Dr. R. Naik, thanks the central instrumentation facility of ICT-IOC for different characterizations and the Science and Engineering Research Board (SERB), Govt. of India for financial support (CRG/2022/003084). The J.K. acknowledge the High-Performance

Computing (HPC) facility provided by the Center of Excellence in High Energy and Condensed Matter Physics, Department of Physics, Utkal University, India.

[View Article Online](#)
DOI: 10.1039/D5NA01136A

References:

- 1.D. Alagarasan, S. S. Hegde, R. Naik, P. Murahari, H. D. Shetty, F. H. Alkallas, A. B. G. Trabelsi, F. S. Khan, S. AlFaify, M. Shkir, Fabrication of Bi-doped In_2S_3 thin films for highly sensitive UV photodetector applications, *J. Photo Chem. Photo Bio. A: Chem.* 454 (2024) 115697.
- 2.Q. Huang, J. Zhu, F. Qi, L. Zhang, F. Chen, Y. Pu, N. Zhang, M. Wang, W. Chen, X. Tang, Ultraviolet–Visible Photodetector Based on a Cs_2TeI_6 Thin Film, *ACS Appl. Electron. Mater.* 7 (2025) 910–918
- 3.G. Mallick, P.C. Kumar, R. Naik, R. Biswal, Enhanced photoresponse from $\text{Ag}/\text{Bi}_2\text{Se}_3$ heterostructure thin films under thermal annealing, *ACS Appl. Electron. Mater.* 7 (12), (2025) 5583–5598.
- 4.D. Alagarasan, S. S. Hegde, A. Kumar, B. Shanmugavelu, P. Murahari, R. Ganesan, R. Naik, M. Ubbaidullah, M. Gupta, B. Pandit, N. Senthilkumar, S. S. Sehgal, Influence of La^{3+} doping on nebulizer spray pyrolysed In_2S_3 thin film for enhanced photodetector performance, *J. Photochem. Photobio. A: Chem.* 444 (2023) 114941.
- 5.A. Parida, D. Alagarasan, R. Naik, High-performance, fast-response photodetector based on hydrothermally synthesized $\text{V}_{1-x}\text{MoxSe}_2$ nanosheets, *Dalton Transact.* 54 (2024) 1111-1126.
- 6.L. Mahapatra, P. C. Kumar, P. Pradhan, D. Alagarasan, C. Sripan, R. Naik, High photo detectivity, responsivity under time-dependent laser-irradiation of $\text{Cu}_{40}\text{Sb}_{40}\text{S}_{20}$ thin films for photodetector application, *Mater. Adv.* (2025) DOI: 10.1039/D5MA00505A
- 7.H. Chen, K. Liu, L. Hu, A. A. Al-Ghamdi, X. Fang, New concept ultraviolet photodetectors, *Mater. Today*, 18 (9), (2015) 493-502.
- 8.D. Alagarasan, S. S. Hegde, B. Shanmugavelu, R. Aadhavan, R. Naik, Hitha D. Shetty, V. Ganesh, H. Algarni, R. Ganesan, Fabrication of SnSe nanostructures visible light photodetectors, *Inorg. Chem. Commun.* 170 (2024) 113276.
- 9.Z. Zheng, J. Yao, B. Wang, Y. Yang, G. Yang, J. Li, Self-assembly high-performance UV–vis–NIR broadband $\beta\text{-In}_2\text{Se}_3/\text{Si}$ photodetector array for weak signal detection, *ACS Appl. Mater. Interfaces*, 9 (2017) 43830–43837.
- 10.S. S. Kumar, S. Valanarasu, R. S. Rimal Isaac, A. V. Juliet, V. Ganesh, Effect of substrate temperature on In_2S_3 thin films using nebulizer spray pyrolysis method for photodetector applications, *Phys. Scr.* 99 (2024) 115936.

11. L. Li, Q. Wu, C. Wang, Z. Cai, L. Lin, X. Gu, K. K. Ostrikov, H. Nan, S. Xiao, High-performance InSe photodetector induced by synergetic surface plasmon resonance and surface engineering, *ACS Photonics*, 11(7), (2024) 2615–2623.

12. C. Jia, S. Wu, J. Fan, C. Luo, M. Fan, M. Li, L. He, Y. Yang, H. Zhang, Ferroelectrically modulated and enhanced photoresponse in a self-powered α -In₂Se₃/Si heterojunction photodetector, *ACS Nano*, 17(7), (2023) 6534–6544.

13. H. Li, K. Zhang, X. Li, B. Liu, L. Li, Z. Mei, T. Chen, Q. Liu, W. Yu, J. Yuan, H. Mu, S. Lin, Two-dimensional (2D) α -In₂Se₃/Ta₂NiSe₅ heterojunction photodetector with high sensitivity and fast response in a wide spectral range, *Mater. Design*, 227 (2023) 111799.

14. Y. Zhao, F. Guo, R. Ding, W. F. Io, Sin-Yi Pang, W. Wu, J. Hao, Piezo-phototronic effect in 2D α -In₂Se₃/WSe₂ van der Waals heterostructure for photodetector with enhanced photoresponse, *Adv. Opt. Mater.* 9 (2021) 2100864.

15. Y. Hase, M. Prasad, P. Shinde, S. Shah, A. Punde, V. Doiphode, S. Rahane, S. Ladhan, D. Kale, A. Waghmare, B. Bade, S. P. Patole, S. Jadkar, Self-powered γ -In₂Se₃/p-Si heterojunction for photodetection: exploring humidity and light intensity dependent photo response, *Opt. Express*, 32 (2024) 38258–38274.

16. F. Wang, L. Zhang, H. Deng, A. T. S. Wee, High-Performance Photoresponse and nonvolatile photomemory effect in a partially gated MoS₂/ α -In₂Se₃ heterojunction photodetector, *ACS Appl. Mater. Interfaces*, 17 (2025) 31087–31095.

17. B. Liu, B. Tang, F. Lv, Y. Zeng, J. Liao, S. Wang, Q. Chen, Photodetector based on heterostructure of two-dimensional WSe₂/In₂Se₃, *Nanotechnology*, 31 (2020) 065203.

18. P. Li, T. Wang, A. Wang, L. Zhao, Y. Zhu, Z. Wang, H. Gao, W. Wang, K. Li, C. Du, Carrier-recirculating broadband photodetector with high gain based on van der Waals In₂Se₃/MoS₂ heterostructure, *Appl. Surf. Sci.* 649 (2024) 159135.

19. S. V. Solanke, R. Soman, M. Rangarajan, S. Raghavan, D. N. Nath, UV/Near-IR dual band photodetector based on p-GaN/ α -In₂Se₃ heterojunction, *Sensors and Actuators A: Physical*, 317 (2021) 112455.

20. Y. Hase, P. Kolhe, V. Doiphode, A. Punde, P. Shinde, S. Rahane, D. Kale, S. Shah, S. Ladhan, M. Prasad, S. Dahiwale, M. Z. A. Yahya, S. Jadkar, Enhanced photodetection performance of self-biased γ -In₂Se₃/p-Si heterojunction photodetectors using argon ion irradiation, *J. Mater. Sci: Mater. Electron.* 35 (2024) 1642.

21. H. Li, J. Yuan, Q. Liu, H. Mu, Self-powered In₂Se₃/PtSe₂ photodetector with broadband and fast response, *Mater. Lett.* 344 (2023) 134425.

22. D. Alagarasan, S. S. Hegde, S. Varadharajaperumal, K. D. Arun Kumar, R. Naik, S. P. Panjalingam, E. El Sayed Massoud, R. Ganesan, Effect of annealing temperature on SnS thin films for photodetector applications, *J. Mater. Sci: Mater. Electron.* 33 (2022) 4794–4805.

23. P. C. Kumar, S. Mohanty, J. Panda, S. Das, S. Supriya, D. Alagarasan, R. Naik, Enhanced photoresponse in a $\text{Ag}_2\text{S}/\text{In}_2\text{Se}_3$ heterojunction based visible light photodetector, *RSC Adv.* 15 (2025) 14518–14531.

24. S. Das, D. Alagarasan, S. Varadharajaperumal, R. Ganesan, R. Naik, Tuning the nonlinear susceptibility and linear parameters upon annealing $\text{Ag}_{60-x}\text{Se}_{40}\text{Te}_x$ nanostructured films for nonlinear and photonic applications, *Mater. Adv.*, 3 (2022) 7640–7654.

25. D. Alagarasan, S. S. Hegde, S. Varadharajaperumal, K. D. A. Kumar, R. Naik, S. P. Panjalingam, M. E. El Sayed Massoud and R. Ganesan, Effect of annealing temperature on SnS thin films for photodetector applications, *J. Mater. Sci.: Mater. Electron.*, 2022, **33**, 4794–4805.

26. S. Thaowonkaew, M. Insawang, A. Vora-ud, M. Horprathum, P. Muthitamongkol, S. Maensiri, M. Kumar, T. B. Phan, T. Seetawan, Effect of substrate rotation and rapid thermal annealing on thermoelectric properties of Ag-doped Sb_2Te_3 thin films, *Vacuum*, 211 (2023) 111920.

27. M. Ganaie, M. Zulfequar, Optical and electrical properties of $\text{In}_4\text{Se}_{96-x}\text{S}_x$ chalcogenide thin films, *J. Alloys Compd.*, 687 (2016) 643–651.

28. A. A. A. Darwish, M. M. El-Nahass, M. H. Bahlol, Structural and electrical studies on nanostructured InSe thin films, *Appl. Surf. Sci.*, 276 (2013) 210–216.

29. F. Zakerian, H. Kafashan, Investigation of the effect of annealing parameters on the physical properties of electrodeposited ZnS thin films, *Superlattices Microstruct.*, 124 (2018) 92–106.

30. E. R. Shaaban, M. Mohamed, M. N. Abd-el Salam, A. Y. Abdel-Latif, M. A. Abdel-Rahim, E. S. Yousef, Structural, linear and nonlinear optical properties of annealed $\text{As}_{47.5}\text{Se}_{47.5}\text{Ag}_5$ thin films for optoelectronic applications, *Opt. Mater.* 86 (2018) 318–325.

31. B. T. Mukherjee, M. Saxena, Y. K. Kuo, G. S. Okram, S. Dam, S. Hussain, A. Lakhani, U. Deshpande, T. Shripathi, Ag-Nanoinclusion-Induced enhanced thermoelectric properties of Ag_2S , *ACS Appl. Energy Mater.*, 2(9), (2019) 6383–6394.

32. J. Munaro, P. Dolcet, S. Nappini, E. Magnano, N. Dengo, G. Lucchini, A. Speghini, S. Gross, The role of the synthetic pathways on properties of Ag_2S nanoparticles for photothermal applications, *Appl. Surf. Sci.*, 514 (2020) 145856.

New Article Online
DOI: 10.1039/DNA01136A



33. V. D. Botcha, Y. Hong, Z. Huang, Z. Li, Q. Liu, J. Wu, Y. Lu, X. Liu, Growth and thermal properties of various In_2Se_3 nanostructures prepared by single step PVD technique, *J. Alloys Compd.*, 773 (2019) 698-705.

34. S. Das, S. Senapati, G. K. Pradhan, S. Varadharajaperumal, R. Naik, A facile microwave-assisted nanoflower-to-nanosphere morphology tuning of $\text{CuSe}_{1-x}\text{Te}_{1+x}$ for optoelectronic and dielectric applications, *ACS Appl. Nano Mater.* 6(7), (2023) 5298-5312.

35. S. Das, B. Dandasena, D. Alagarasan, R. Naik, Enhanced photoresponse and surface wettability of Bi_2Se_3 film with annealing at different temperatures for optoelectronic applications, *ACS Appl. Opt. Mater.* 2 (4), (2024) 642-654.

36. P. Priyadarshini, Prabhukrupa C. Kumar, R. Naik, Tuning in optoelectronic properties of In/Te bilayer heterostructure upon annealing at different temperatures: Surface wettability and photo response study for photonic and solar cell applications, *RSC Adv.* 14 (2024) 12897.

37. S. K. Sethi, G. Manik, Recent progress in super hydrophobic/hydrophilic self-cleaning surfaces for various industrial applications: A review, *Polymer-Plastics Techn. Eng.* 57, (2018) 1932-1952.

38. D. Ahmad, I. van den Boogaert, J. Miller, R. Presswell, H. Jouhara, Hydrophilic and hydrophobic materials and their applications, *Energy Sources, Part A: Recovery, Utilization, and Environmental Effects*, 40(22), (2018) 2686-2725.

39. R. Naik, S. Jena, R. Ganesan, N.K. Sahoo, Laser-induced optical properties change in $\text{Sb}_{10}\text{S}_{40}\text{Se}_{50}$ chalcogenide thin films: An investigation through FTIR and XPS measurements, *Physica Status Solidi (b)* 251 (3), (2014) 661-668.

40. M.S. Ebied, A.F. Elhady, M. Dongol, A.A. Abuelwafa, Thermal annealing induced modification in linear and nonlinear optical properties of $\text{Ag/Ge}_{20}\text{Se}_{50}\text{S}_{30}$ bilayer film, *Opt. Mater.* 148 (2024) 114962.

41. R. Chauhan, Y. A.M. Ismail, K. A. Aly, P. Sharma, R. Sharma, C. Tyagi, S. Sharda, Optical properties and structural rigidity of $[(\text{GeSe}_2)_{75}(\text{Sb}_2\text{Se}_3)_{25}]_{100-x}\text{Te}_x$ chalcogenide glasses for potential applications in infrared filters and lenses, *J. Mater. Sci: Mater. Electron.* 35 (2024) 1698.

42. P. Priyadarshini, D. Alagarasan, R. Ganesan, S. Varadharajaperumal, R. Naik, Influence of proton ion irradiation on the linear–nonlinear optoelectronic properties of $\text{Sb}_{40}\text{Se}_{20}\text{S}_{40}$ thin films at different fluences for photonic devices, *ACS Appl. Opt. Mater.* 1 (1), (2023) 55-68.

43. J. Tauc, *Amorphous and liquid semiconductors*, Plenum Press, New York, NY, USA, 1979.

44. X. Chai, R. Guzman, Y. Zhou, Z. Xu, Z. Liang, Y. Zhu, W. Zhou, J. Chen, *New Article Online* DOI: 10.1039/DNA01136A
Interfacial intermixing and its impact on the energy band structure in interband cascade infrared photodetectors, *ACS Appl. Mater. Interfaces*, 13 (2021) 38553–38560.

45. N. F. Mott and E. A. Davis, Electronic processes in non-crystalline materials, in: Clarendon Press, Oxford, 1979, 210.

46. F. Urbach, The long-wavelength edge of photographic sensitivity and of the electronic absorption of solids, *Phys. Rev.*, 92 (1953) 1324.

47. A. R. Zanatta, I. Chambouleyron, Absorption edge, band tails, and disorder of amorphous semiconductors, *Phys. Rev. B*, 53 (1996) 3833.

48. Neetu, M. Zulfequar, Annealing effect on optical parameters of $\text{Se}_{85-x}\text{Te}_{15}\text{Hg}_x$ thin films, *J. Alloys Compd.*, 576 (2013) 103-107.

49. S. Giri, P. Priyadarshini, D. Alagarasan, R. Ganesan, R. Naik, Annealing-induced phase transformation in $\text{In}_{10}\text{Se}_{70}\text{Te}_{20}$ thin films and its structural, optical and morphological changes for optoelectronic applications, *RSC Adv.* 13 (36), (2013) 24955-24972.

50. S. Moustafa, M. Mohamed, M. A. Abdel-Rahim, Composition dependence of structural and optical properties of $\text{Ge}_x\text{Se}_{100-x}$ semiconducting thin films, *Opt. Quantum Electron.*, 51 (2019) 1–19.

51. J. A. Duffy, Trends in energy gaps of binary compounds: an approach based upon electron transfer parameters from optical spectroscopy, *J. Phys. C Solid State Phys.*, 13 (1980) 2979.

52. V. Dimitrov and S. Sakka, Linear and nonlinear optical properties of simple oxides. II, *J. Appl. Phys.*, 79 (1996) 1741.

53. I. Sharma, P. Sharma and A. S. Hassanien, Optical properties and optoelectrical parameters of the quaternary chalcogenide amorphous $\text{Ge}_{15}\text{Sn}_x\text{S}_{35-x}\text{Te}_{50}$ films, *J. Non-Cryst. Solids*, 590 (2022) 121673.

54. T. S. Moss, A relationship between the refractive index and the infra-red threshold of sensitivity for photoconductors, *Proc. Phys. Soc. Sec.*, 63(1950) 167–176.

55. H. Nyakoto, T. S. Sathiaraj and E. Muchuweni, Effect of annealing on the optical properties of amorphous $\text{Se}_{79}\text{Te}_{10}\text{Sb}_4\text{Bi}_7$ thin films, *Opt. Laser Technol.*, 92 (2017) 182–188.

56. P. Herve and L. K. J. Vandamme, General relation between refractive index and energy gap in semiconductors, *Infrared Phys. Technol.*, 35 (1994) 609–615.

57. S. K. Tripathy, Refractive indices of semiconductors from energy gaps, *Opt. Mater.* 46 (2015) 240–246.

58. M. Sulaman, Y. Song, S. Yang, M. Li, M. I. Saleem, P. V. Chandrasekar, Y. Jiang, Y. Tang, B. Zou, Ultra-sensitive solution-processed broadband photodetectors based on vertical field-effect transistor, *Nanotechnology*, 31 (2020) 105203.

59. Z. Q. Zheng, J. D. Yao, G. W. Yang, Growth of centimeter-scale high-quality In_2Se_3 films for transparent, flexible and high-performance photodetectors, *J. Mater. Chem. C*, 4 (2016) 8094-8103.

60. S. Rajeswari, M. M. Ibrahim, A. M. Al-Enizi, M. Ubaidullah, P. Arunachalam, B. Pandit, S. F. Shaikh, Photo-sensing properties of Cd-doped In_2S_3 thin films fabricated via low-cost nebulizer spray pyrolysis technique, *J. Mater. Sci. Mater. Electron.*, 33 (2022) 19284–19296.

61. S. S. Kumar, S. Valanarasu, R. R. Isaac, A.V. Juliet, V. Ganesh, Effect of substrate temperature on In_2Se_3 thin films using nebulizer spray pyrolysis method for photodetector applications. *Phys. Scr.*, 99(11) (2024) 115936.

62. P. C. Kumar, S. Kanungo, P. Pradhan, S. K. Biswal, J. Kumar, C. Sripan, R. Naik, Tuning hydrophilicity and photoresponse by interfacial Ag diffusion in the Sb_2S_3 layer for optoelectronic applications: An experimental and computational study, *J. Phys. Chem. C*, 128(39), (2024) 16740-16753.

63. G. Kresse, J. Furthmüller, Efficient iterative schemes for ab initio total-energy calculations using a plane-wave basis set, *Phys. Rev. B*, 54 (1996) 11169.

64. G. Kresse, J. Furthmüller, Efficiency of ab-initio total energy calculations for metals and semiconductors using a plane-wave basis set, *Comput. Mat. Sci.*, 6 (1996) 15-50.

65. K. Momma, F. Izumi, VESTA 3 for three-dimensional visualization of crystal, volumetric and morphology data, *J. Appl. Cryst.*, 44 (2011) 1272-1276.

66. J. P. Perdew, K. Burke, M. Ernzerhof, Generalized gradient approximation made simple, *Phys. Rev. Lett.*, 77 (1996) 3865.

View Article Online
DOI: 10.1039/D5NA01136A



Data Availability Statement

[View Article Online](#)
DOI: 10.1039/D5NA01136A

Title of Manuscript: *Diffusion-Induced Enhanced Photoresponsivity, Detectivity in Ag_2S and In_2Se_3 Heterostructure for UV-Visible Photodetector: An Experimental and Computational Analysis*

Corresponding Authors: Dr. Ramakanta Naik

- All data needed to support the conclusions in the paper are presented in the manuscript and the Electronic Supplementary Material. Additional data related to this paper may be requested from the corresponding author upon request.
- The data are plotted in with the help of Origin software.
- Analysis and quantification of images were performed using ImageJ software.